

A CH_3CN and HCO^+ survey towards southern methanol masers associated with star formation

C. R. Purcell¹, R. Balasubramanyam^{1,2}, M. G. Burton¹, A. J. Walsh¹, V. Minier^{1,3,4}, M. R. Hunt-Cunningham¹, L. L. Kedziora-Chudczer^{1,6}, S. N. Longmore^{1,5}, T. Hill¹, I. Bains¹, P. J. Barnes^{1,6}, A. L. Busfield⁷, P. Calisse^{1,8}, N. H. M. Crighton¹, S. J. Curran¹, T. M. Davis^{1,9}, J. T. Dempsey¹, G. Derragopian¹, B. Fulton^{1,10}, M. G. Hidas¹, M. G. Hoare⁷, J.-K. Lee^{1,11}, E. F. Ladd^{12,1,5}, S. L. Lumsden⁷, T. J. T. Moore¹³, M. T. Murphy^{1,14}, R. D. Oudmaijer⁶, M. B. Pracy¹, J. Rathborne^{1,15}, S. Robertson⁵, A. S. B. Schultz¹, J. Shobbrook¹, P. A. Sparks¹, J. Storey¹, T. Travouillon^{1,16}

¹ School of Physics, University of New South Wales, Sydney, NSW 2052, Australia

² Raman Research Institute, Sadashivanagar, Bangalore 560 080, India

³ Service d'Astrophysique, DAPNIA/DSM/CEA Saclay, 91191 Gif-sur-Yvette, France

⁴ AIM, Unité Mixte de Recherche, CEA–CNRS–Université Paris VII, UMR 7158, CEA/Saclay, 91191 Gif sur Yvette, France

⁵ CSIRO Australia Telescope National Facility, PO Box 76, Epping, NSW 1710, Australia

⁶ School of Physics, University of Sydney, NSW 2006, Australia

⁷ School of Physics and Astronomy, University of Leeds, Leeds LS2 9JT, UK

⁸ School of Physics and Astronomy, University of Wales, Cardiff, 5, The Parade, Cardiff CF24 3YB, Wales, UK

⁹ Research School of Astronomy and Astrophysics, The Australian National University, Mount Stromlo Observatory, Cotter Road, Weston Creek, ACT 2611, Australia

¹⁰ Centre for Astronomy, James Cook University, Townsville, QLD 4811, Australia

¹¹ Department of Pure and Applied Physics, Queen's University, Belfast BT7 1NN, U.K.

¹² Department of Physics, Bucknell University, Lewisburg, PA 17837, USA

¹³ Astrophysics Research Institute, Liverpool John Moores University, 12 Quays House, Egerton Wharf, Birkenhead CH41 1LD, UK

¹⁴ Institute of Astronomy, University of Cambridge, Madingley Road, Cambridge CB3 0HA, UK

¹⁵ Institute for Astrophysical Research, Boston University, Boston, MA 02215, USA

¹⁶ California Institute of Technology, 1200 E. California Blvd, Pasadena 91125, CA, USA

6 June 2018

ABSTRACT

We present the initial results of a 3-mm spectral line survey towards 83 methanol maser selected massive star-forming regions. Here we report observations of the $J=5-4$ and $6-5$ rotational transitions of methyl cyanide (CH_3CN) and the $J=1-0$ transition of HCO^+ and H^{13}CO^+ .

CH_3CN emission is detected in 58 sources (70% of our sample). We estimate the temperature and column density for 37 of these using the rotational diagram method. The temperatures we derive range from 28–166 K, and are lower than previously reported temperatures, derived from higher J transitions. We find that CH_3CN is brighter and more commonly detected towards ultra-compact H II (UCH II) regions than towards isolated maser sources. Detection of CH_3CN towards isolated maser sources strongly suggests that these objects are internally heated and that CH_3CN is excited prior to the UCH II phase of massive star-formation.

HCO^+ is detected towards 82 sources (99% of our sample), many of which exhibit asymmetric line profiles compared to H^{13}CO^+ . Skewed profiles are indicative of inward or outward motions, however, we find approximately equal numbers of red and blue-skewed profiles among all classes. Column densities are derived from an analysis of the HCO^+ and H^{13}CO^+ line profiles.

80 sources have mid-infrared counterparts: 68 seen in emission and 12 seen in absorption as ‘dark clouds’. Seven of the twelve dark clouds exhibit asymmetric HCO^+ profiles, six of which are skewed to the blue, indicating infalling motions. CH_3CN is also common in dark clouds, where it has a 90% detection rate.

Key words: ISM:molecules — stars:formation — H II regions — radio lines:ISM —

1 INTRODUCTION

Identifying young massive stars ($> 8 M_{\odot}$) in their early evolutionary phases is an important step in attempting to understand massive star formation and its effect on the Galactic ecology.

Massive stars begin their lives at the centre of dense contracting cores, embedded in giant molecular clouds (GMCs). At the earliest stages of their evolution they heat the surrounding dust, and are visible as luminous sub-millimetre (mm) and far-infrared sources (Kurtz et al. 2000). High densities existing prior to the final collapse cause simple organic molecules present in the interstellar medium to freeze onto the dust mantles. Grain surface chemistry leads to the production of heavy ices such as methanol (CH_3OH). As the protostar evolves, heat and radiation evaporate these species, expelling them into gas phase where they fuel a rich ‘hot core’ chemistry (van Dishoeck & Blake 1998). Eventually, the embedded protostar ionises the surrounding environment, forming a ultra-compact HII (UCHII) region and complex molecules are destroyed owing to continued exposure to heat and radiation.

Targeted surveys towards known star forming regions have suggested a close relationship between class II methanol masers, hot cores and UCHII regions (Menten 1991; Minier et al. 2001). Parkes 64-m and Australia Telescope Compact Array (ATCA) observations by Walsh et al. (1998, 1999) have shown that only 25 % of methanol masers are directly associated with radio continuum emission, tracing UCHII regions. Subsequent follow-up observations towards the *isolated* masers confirm that all maser sites are associated with luminous sub-mm continuum emission (Walsh et al. 2003).

In the present paper we investigate the link between methanol masers, UCHII regions and the chemically active ‘hot molecular core’ (HMC) phase of massive star formation. We present the initial results of a single-dish molecular line survey of 83 methanol maser selected massive star forming regions.

1.1 CH_3CN Spectroscopy

The primary chemical tracer in this survey is methyl cyanide (CH_3CN). CH_3CN is a good tracer of the conditions found in HMCs owing to its favourable abundance and excitation in warm (> 100 K) and dense ($> 10^5 \text{ cm}^{-3}$) regions. It is thought to form through reactions between species evaporated from dust grain mantles (e.g. Millar, MacDonald & Gibb 1997) or through gas phase chemistry in the envelope around massive young stars (see Mackay 1999). Grain-surface chemistry has also been invoked to explain the enhanced abundances observed in HMCs, however, in all formation scenarios CH_3CN is evident in observations after the core temperature rises past ~ 90 K.

CH_3CN is a member of the c_{3v} group of symmetric tops, whose rotational energy levels may be described by two quantum numbers: J , the total angular momentum and K , the projection of J along the axis of symmetry. Individual $J \rightarrow (J-1)$ transitions are grouped into ‘rotational ladders’ labelled by their K values (see Loren & Mundy (1984) for a detailed description). For each $J \rightarrow (J-1)$ transition, selection rules prohibit radiative transitions between the K ladders and their relative populations are determined exclusively by collisional excitation. Assuming local thermal equilibrium (LTE) and optically thin lines, the relative intensities of the K components yield a direct measure of the kinetic temperature and column density.

The energy spacings between individual J levels are almost independent of K ladder, however, increasing centrifugal distortion

causes successive K components to shift to progressively lower frequencies. The offset in frequency is slight, and the K components of a particular $J \rightarrow (J-1)$ transition may be observed simultaneously in a single bandpass, minimising errors in their relative calibration.

Spin statistics of the hydrogen nuclei divide CH_3CN into two spin states, dubbed A and E. Energy levels with $K = 3n$, $n = 0, 1, 2 \dots$ belong to the A state, while those with $K \neq 3n$, $n = 0, 1, 2 \dots$ belong to the E state. The A states have twice the statistical weight of the E states. Neither radiation nor collisions convert between states; if formed in equilibrium conditions the A/E abundance ratio is expected to be ~ 1 (Minh et al. 1993).

1.2 HCO^+ Spectroscopy

HCO^+ and its isotopomer, H^{13}CO^+ , were also observed in order to probe the kinematics of the extended envelopes and as a diagnostic of the optical depth towards the cores. A comparison between the generally optically thick HCO^+ line and the optically thin H^{13}CO^+ line yields information on the bulk motions of gas in the regions.

HCO^+ has a large dipole moment and is a highly abundant molecule, with abundance especially enhanced around regions of higher fractional ionisation. HCO^+ is also enhanced by the presence of outflows where shock generated radiation fields are present (Rawlings, Taylor & Williams (2000); Rawlings et al. (2004)). It shows saturated and self absorbed line profiles around massive star-forming regions and is a good tracer of the dynamics in the vicinity of young protostellar objects (e.g. De Vries & Myers 2005). The emission from its isotopomer, H^{13}CO^+ , is generally optically thin and traces similar gas densities to HCO^+ at $n \sim 10^5 \text{ cm}^{-3}$.

Table 1 presents the details of the observed transitions. All molecular constants are in SI units and come from the catalog of Pickett, et al. (1998).

We justify the source selection criteria and derive the distances and luminosities in the following section. In § 3 we describe the observations and data reduction methodology. In § 4, we present the initial results of the line survey and describe the data. We outline the analysis techniques used and present derived physical parameters in § 5, and in § 6 we analyse and discuss general trends in the data and test the validity of our results. Finally, in § 7 we conclude with a summary of our investigations and suggest future avenues of investigation. The full set of spectra, MSX images and related plots are presented as an online addition to this paper.

2 SOURCE SELECTION

77 sources were drawn from the methanol maser, radio and sub-millimetre surveys conducted by Walsh et al. (1997, 1999, 2003). The original sources were chosen for their red IRAS colours using the colour selection criteria of Wood & Churchwell (1989), to be indicative of UCHII regions. Our sub-sample of 6.71 GHz methanol maser sites are all associated with warm, dusty clumps, traced by sub-millimetre continuum emission (Walsh et al. 2003). The final selection was also constrained by the latitude of the Mopra antenna at -31° . We required that the sources remain above an elevation of 30° for at least three hours between the months June to September so allowed declinations were restricted between 0 and -60 degrees. The sample are split into two main categories: eighteen maser sites are within a Mopra beam ($33''$) of UCHII regions. The remaining

59 maser-sites have no detectable radio emission and are associated only with thermal emission in the sub-mm and infrared. An additional six ‘maserless cores’, only detected in thermal emission, were added to the list, bringing the total sample to 83. These cool dusty clumps were selected from recent 1.2-mm continuum observations by Hill et al. (2005) and are found in the same fields but offset from the masers and radio emission. One such core was subsequently found to be coincident with a UCH_{II} region but the others are not directly associated with other tracers of massive star formation. We investigate the remaining five as potential precursors to the hot core phase.

Table 2 presents the source details and their associations. The first column is the abbreviated Galactic name, columns two and three are the J2000 equatorial coordinates of the pointing centre (usually coincident with the maser site). Column five presents the adopted kinematic distances in kpc. The approximate bolometric luminosity and single-star spectral type are noted in columns six and seven and any associated methanol maser, radio-continuum or mid-infrared thermal emission is noted in column eight. Alternative names used in the literature are presented in the final column.

2.1 Kinematic Distances

The majority of sources are in the first quadrant of the Galactic plane, between longitude (l) 0° and 35° . Five sources are located between $l = 316^\circ$ and 335° . We used the rotation curve of Brand & Blitz (1993) to calculate the kinematic distance, assuming a distance to the Galactic centre of 8.5 kpc and a solar angular velocity of 220 km s^{-1} . In most cases the V_{LSR} was determined from Gaussian fits to the H^{13}CO^+ line.

All sources lie inside the solar circle and thus have a near/far distance ambiguity. We were able to resolve the ambiguity for 58 sources, mainly using the work of Downes et al. (1980), Solomon et al. (1987) and Wink, Altenhoff & Mezger (1982). Also, where the near and far kinematic distances are within ~ 1 kpc we have assigned the distance of the tangent point to the source. We favoured the near distance when a source was seen in absorption in $8 \mu\text{m}$ images. Several sources have been identified in the literature as being part of the same complex and we have placed them at a common distance. The remaining 25 sources are assumed to lie at the near kinematic distance, except for G10.10+0.72, which was not convincingly detected in any molecular tracer and was placed at the far distance.

Assuming peculiar velocities $\pm 10 \text{ km s}^{-1}$ from the model Galactic rotation curve, we estimate the error in the distance is 0.65 ± 0.29 kpc, or $20 \pm 9\%$ of the near kinematic distance. Eighteen sources in our sample lie between $l=0^\circ$ and $l=10^\circ$. Over these longitudes the Galactic rotation curve is not well determined and large peculiar velocities will lead to correspondingly greater errors in the distance determination.

2.2 Bolometric luminosities

If we assume the millimetre, sub-millimetre, far and near infrared emission is associated with the same object, we can estimate a bolometric luminosity by fitting a two-component greybody to the spectral energy distribution (SED) (e.g. Faúndez et al. 2004; Minier et al. 2005 and references therein). The model greybody SED is a summation of two blackbodies, with separate temperatures and amplitudes, modified by a common dust emissivity index, β . Typical values for β range between one and two, with

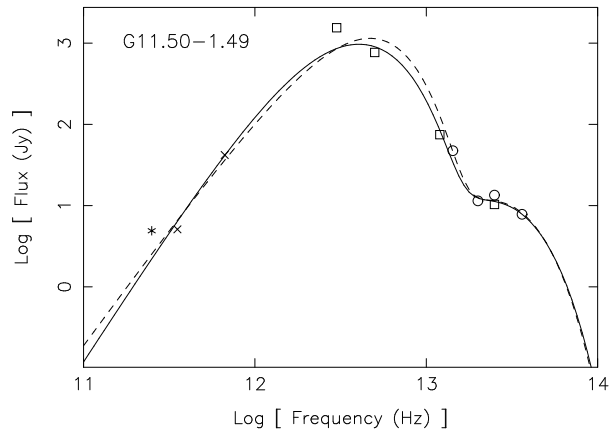


Figure 1. Greybody fits to the SED of source G11.50–1.49. MSX data points are plotted as circles, IRAS data points are plotted as squares, SCUBA data points are plotted as crosses and SIMBA data points are plotted stars. The solid line represents a two-component fit to all data points, while the dashed line represents a fit to the SIMBA, SCUBA and MSX data only. Without the IRAS points the fit overestimates the integrated intensity by a factor of 1.5 ± 0.8 . The bolometric luminosity is estimated to be accurate to a within a factor of two.

the Kramers-Kroing theorem constraining the lower limit at one (Emerson 1988). In the literature a value of two is generally assumed (Dunne et al. 2000; James et al. 2002; Kramer et al. 2003) and recent results by Hill et al. (in preparation) suggest an emissivity of two for a sample of massive star forming regions. Accordingly we limit β between values of one and two for our fits, while all other parameters are free. No attempt was made to interpret the greybody fits, except to measure the total intensity by integrating under the curve between 10^6 and 10^{16} Hz.

Sub-millimetre data for 78 maser sites comes from the observations of Walsh et al. (2003) using the SCUBA bolometer on the James Clerk Maxwell Telescope (JCMT). 1.2-mm fluxes were taken from the work of Hill et al. (2005). Far and mid-infrared fluxes are drawn from the Infrared Astronomy Satellite (IRAS) point source catalog¹ and measured directly from the Midcourse Space Experiment (MSX) images. We have assumed 30% errors on all fluxes.

High source multiplicity in the Galactic plane means quoted IRAS fluxes may contain contributions from several sources within the $1'$ IRAS beam. We include IRAS data in the SED if the source appears isolated in the higher resolution MSX image, or if the MSX and IRAS fluxes match at $14 \mu\text{m}$. In some cases the 60 and $100 \mu\text{m}$ points are included as upper limits to the fit. Without data points at $\sim 100 \mu\text{m}$, the peak of the SED is not well constrained. In an attempt to measure the effect of missing data, we fit fifteen SEDs with the IRAS data removed and compared the results to fits utilising the IRAS data. We find that the integrated intensity is, on average, overestimated by a factor of 1.3 ± 0.6 when the IRAS data is absent. An inspection of the fits reveals that when IRAS data is not present the height of the peak depends most strongly on the SCUBA 450 and $850 \mu\text{m}$ data and tends to be exaggerated. Figure 1 shows a typical SED. The solid line is a two-component greybody fit to all points, while the dashed line represents a fit to the data with

¹ IRAS images and photometry data are available online at <http://www.ipac.gov.com>

the IRAS points removed. Plots of the greybody fits to all sources are available in the online version of this work.

The percentage error in the fit adds in quadrature to twice the error in the distance, leading to a luminosity determined to within a factor of ~ 2 in most cases.

3 OBSERVATIONS AND DATA REDUCTION

3.1 The Mopra mm-wave observatory

The Australia Telescope National Facility (ATNF) ‘Mopra’ telescope is a 22-m antenna located 26 km outside the town of Coonabarabran in New South Wales, Australia. At an elevation of 850 metres above sea level and a latitude of 31° south, it is ideally placed for observations of the southern Galactic plane.

The receiver is comprised of a set of cryogenically cooled low-noise SIS mixers, capable of operating at frequencies between 85 and 115 GHz. A polarisation splitter divides the beam into two orthogonal linear polarisations (A and B), which are processed separately. The system is usually configured for dual-polarisation observations, with both polarisations tuned to the same sky frequency, however, polarisation B can be independently tuned to a dedicated ‘pointing’ frequency at the 86.243 GHz masing transition of SiO. A digital auto-correlator forms the back-end, providing each polarisation with available bandwidths ranging from 4 to 256 MHz, which can be split into a maximum of 4096 channels.

The antenna is a Cassegrain design with a 22-m parabolic surface shaped to maximise the forward gain. In a study performed by Ladd et al. (2005) the half-power main-beam size was found to vary between $36 \pm 3''$ and $33 \pm 2''$ over the frequency range 85–115 GHz. The main-beam efficiency varied from 0.49 ± 0.03 to 0.42 ± 0.02 over the same range. Sources with angular extent $< 80''$ couple well to the Gaussian main beam; however, the first error lobe, which extends from diameters of $80''$ to $160''$ contains $\sim 1/3$ of the power present in the main beam and a separate set of efficiencies must be used for calibration of extended sources. We have assumed all sources just fill the main beam and have corrected all of our data onto the main beam temperature scale.

For single pointing surveys the only mode of observation offered is position switching, where the telescope alternates between the science object and an emission-free sky position.

Further technical details on the design of the antenna and receiver systems can be found in the Special Edition of the Journal for Electrical and Electronic Engineering, Australia, Vol 12, No 2, 1992.

3.2 The MSX satellite

The MSX satellite was launched in 1995 by the US Ballistic Missile Defence Organisation with the principal aim of performing a census of the mid-infrared sky. The telescope has a 35-cm clear aperture feeding the SPIRIT-III infrared camera, which has a spatial resolution of $18.3''$. Four wavebands dubbed A, C, D and E are useful for astronomical research and lie at 8, 12, 14 and 21 μm , respectively. Band A (6.8–10.8 μm) is the most sensitive of the four filters but is contaminated by emission from the strong silicate band at 9.7 μm and the polycyclic aromatic hydrocarbon (PAH) band at 8.6 μm . Band E (17.2–27.1 μm) is less sensitive by a factor of ~ 20 than A, and is directly analogous to the broad IRAS 25 μm filter. The instrumentation and survey is described in detail by Egan & Price (1996). Calibrated images of the galactic plane on

a common grid are freely available from the on-line MSX image server at the IPAC archive website at: <http://irsa.ipac.caltech.edu/>.

3.3 Observations

We observed our sample using the 92 GHz $J=5-4$ and 110 GHz $J=6-5$ transitions of CH_3CN as well as the 89 and 86 GHz $J=1-0$ transitions of HCO^+ and H^{13}CO^+ .

The observations reported here were performed as part of a larger survey using the Mopra antenna, conducted over 5 years, from 2000–2004, and between the months May–September. We observed primarily in the dual-polarisation mode. Each polarisation spanned an identical bandwidth of 64 MHz split into 1024 channels, resulting in a velocity resolution of $\sim 0.2 \text{ km s}^{-1}$ over a range of $\sim 180 \text{ km s}^{-1}$. Typical system temperatures ranged from 150 K to 350 K over the course of the observations. Position switching was employed to subtract the sky contribution and bandpass, with emission-free reference positions chosen at declination offsets greater than $10'$. In the few cases where evidence of emission was seen in the reference position, new positions were selected greater than 1° away from the Galactic plane. The pointing accuracy was checked at hourly intervals by observing bright SiO masers of known position and is estimated to be better than $10''$. The pointings towards five sources were consistently off by between 5 and $15''$, due to an error in the observing schedule file. G5.89–0.39 and G19.70–0.27 are offset by $5''$, G29.98–0.04 is offset by $10''$ and G29.96–0.02 is offset by $15''$. The measured brightness temperature will be diminished by an unknown factor in these sources.

A single-load chopper wheel was used to calibrate the data onto a T_A^* scale (see Kutner & Ulich 1981). At Mopra this was implemented by means of a single ambient temperature blackbody paddle placed in front of the beam every few minutes. The data were further calibrated onto a main beam temperature scale (T_{MB}) by dividing by the main beam efficiencies quoted in Ladd et al. (2005).

The typical RMS noise on the T_{MB} calibrated CH_3CN spectra is 80 mK for integrations on-source of approximately 30 minutes. Integration times of 5 and 15 minutes lead to a RMS noise of $\sim 200 \text{ mK}$ and $\sim 100 \text{ mK}$ in the HCO^+ and H^{13}CO^+ spectra, respectively.

3.4 Data Reduction

3.4.1 Mopra spectral line data

Raw data in *rpfits* format were initially reduced using the SPC^{2, 3} package developed by the ATNF and custom routines used to correct for errors in the headers⁴. During the reduction, the spectra were sky-subtracted and the two polarisations averaged together before a low order polynomial was subtracted from the baseline. The reduced data were then read in to the XS⁵ package where

² <http://www.atnf.csiro.au/software/>

³ A tcl/tk user interface to SPC known as Data From Mopra (DFM) is available from <http://www.phys.unsw.edu.au/mopra/software/>

⁴ During 2000–2003 Mopra suffered from a rounding error in the receiver control software which lead to an incorrect velocity scale in the data. A pre-processing script for correcting the data is available from the ATNF Mopra website: <http://www.mopra.atnf.csiro.au>

⁵ XS is written by Per Bergman at the Onsala Space Observatory and is available via FTP on request.

higher order polynomials or sine waves were subtracted if necessary. Finally all the data were converted into the CLASS⁶ format and the spectra were divided by the year-to-year efficiency, η_{yr} , before calibrating onto the main beam brightness temperature (T_{MB}) scale.

3.4.2 Mid-infrared data

Individual 8 and 21 μm images centred on the methanol maser position were acquired from the MSX image server. The MSX images have a stated positional accuracy of $10''$. In an effort to improve registration between datasets, we have utilised the 2MASS near-IR images, which have a pointing accuracy generally better than $1''$. If a constant offset was observed between two or more bright sources present in both data sets, we shifted the MSX coordinates to match those of the 2MASS images. We considered a maser site or UCHII region to be associated with a MSX source if it fell within $9''$ (half of the full-width at half-maximum (FWHM) of the MSX point spread function) of the peak of the infrared source. The MSX fields often suffered from confusion and blending, especially at 8 μm . Where possible, we measured the integrated intensity by drawing a polygon around the source and summing the pixel values. A pixel-averaged sky value was measured from an emission-free region and subtracted from the resulting figure to find the net integrated flux in units of $\text{W m}^{-2} \text{sr}^{-1}$. Conversion to Janskys ($\text{W m}^{-2} \text{Hz}^{-1} \times 10^{26}$) was achieved by dividing by the bandwidth of the filter, and multiplying by the $6 \times 6''$ pixel area in steradians (8.4615×10^{-10} Sr). An additional multiplicative factor of 1.113 was required to correct for the Gaussian response of the individual pixels (Egan & Price 1996). The final scaling factors to convert fluxes in $\text{W m}^{-2} \text{sr}^{-1}$ to Jy were: 6.84×10^3 , 2.74×10^4 , 3.08×10^4 and 2.37×10^4 for the four bands A, C, D and E respectively. On inspection of the 8 μm images we suspect much of the extended emission seen is due PAHs. If a clear distinction was evident between the source and the extended emission, we measured the sky value from average level of the extended emission close to the source.

4 RESULTS

4.1 Spectral line detections

We present a summary of the lines detected towards our sources in Table 3. $\text{CH}_3\text{CN}(5-4)$ emission was detected towards 58 sources (70%), 43 of which are new detections. We followed up the $\text{CH}_3\text{CN}(5-4)$ detections in 33 sources by searching for the 110 GHz $\text{CH}_3\text{CN}(6-5)$ transition and detected the line in 24. HCO^+ was detected towards 82 sources (99%), and H^{13}CO^+ was detected towards 80 sources (98%). Detected spectral lines peak at least $2\text{-}\sigma$ above the baseline and in most cases have a signal to noise ratio greater than four.

Figure 2 presents example spectra for the bright source G0.55+0.85 alongside the 21 μm MSX image. Annotated on the MSX image are the positions of the methanol masers (crosses) and the $36''$ FWHM size of the Mopra beam at 86 GHz (circle). Squares mark the peaks of the compact 8 GHz continuum emission detected by Walsh et al. (1998). Spectra and MSX images for all sources are available as additional online material.

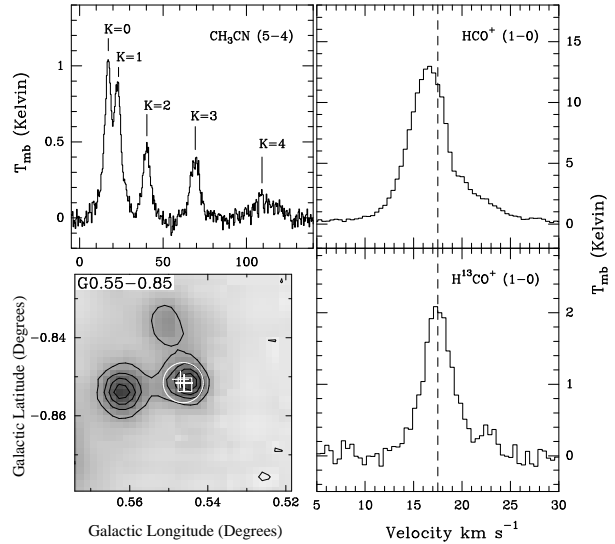


Figure 2. CH_3CN , HCO^+ and H^{13}CO^+ spectra for the bright source G0.55+0.85 alongside the 21 μm MSX image (grey-scale & contours). On the image squares mark known UCHII regions and crosses mark 6.7 GHz methanol-maser sites. The circle shows the $36''$ Mopra beam, centred on the maser position. The CH_3CN K-components are well fit by Gaussians, except for the K=4 line, which may be affected by baseline instabilities. The dashed line marks the V_{LSR} , taken from a Gaussian fit to the H^{13}CO^+ line. The HCO^+ line profile is asymmetric and blue-shifted with respect to the H^{13}CO^+ line, possibly indicating in-falling gas motions.

Individual components within the CH_3CN K-ladder were fit simultaneously with multiple Gaussians. The separations were fixed to their theoretical values and the linewidths constrained to have the same value in the fit. Table 4 lists the Gaussian parameters of the fits to both the $\text{CH}_3\text{CN}(5-4)$ and $(6-5)$ lines. Column one is the Galactic source name, columns two and three are the V_{LSR} and FWHM, columns four to eight contain the fluxes, in K km s^{-1} , of the K=0 to K=4 rotational ladder components. Quoted 1σ uncertainties in the fits are those reported by the CLASS analysis package used to fit the data. The 1σ noise on the spectra of sources without detected $\text{CH}_3\text{CN}(5-4)$ are given in Table 5.

Absolute calibration errors were estimated from multiple observations of individual sources and are generally on the order of 30%. The low signal to noise ratios in many spectra made identification of asymmetries or line wings difficult and we assume the individual K lines were well fit by Gaussians. During our analysis we found that the K=4 component of the $\text{CH}_3\text{CN}(5-4)$ spectrum was almost always anomalously strong and sometimes appeared shifted lower in frequency with respect to the other components. It is possible we are beginning to see excitation by higher temperature gas within the hot core, however, the signal to noise ratio for almost all the K=4 detections is very low and in many cases broad features are seen which have no counterpart in the other K-components, indicating possible baseline problems.

In most cases the detected H^{13}CO^+ lines are well fit with a single Gaussian line, show little evidence of self absorption or line wings, and are assumed to be optically thin. In contrast, the HCO^+ profiles are complex, often exhibiting two or more components (e.g. G8.68-0.37). These profiles may be interpreted as either multiple clouds along the line of sight or a single broad emission line with a self-absorption dip. In an attempt to distinguish between these two cases we examined the profiles for evidence of

⁶ CLASS is part of the GILDAS data reduction package available at <http://www.iram.fr/IRAMFR/GILDAS/>

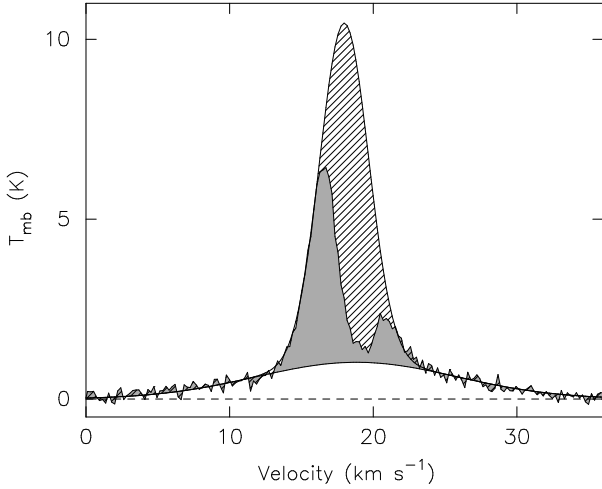


Figure 3. An illustration showing the different methods of measuring the self-absorbed HCO^+ line profiles. We measure the line intensity by integrating under the profile (grey area) and by fitting a Gaussian, constrained by the sides of the line and the velocity of the optically thin H^{13}CO^+ (hatched + grey area). The contribution from high velocity outflow-wings are omitted from both measurements.

multiple components. Where a single H^{13}CO^+ component was visible at the velocity of the dip in the HCO^+ line we attempted to fit the double-peaked profile with a single Gaussian, based on the assumption that the line was strongly self-absorbed. In practice, we blanked the absorption dip from the fitting routine so that the Gaussian fit was constrained only by the sides of the line. At best this gives an upper limit to the intensity of the line. As a lower limit we measured the integrated intensity under the line-profile, after subtracting Gaussian fits to any line wings. Figure 3 illustrates this method using the extreme case of G16.86–2.16. The results of these measurements are reported in Table 6.

Twenty-six sources detected in HCO^+ have residual line wings distinct from the main line, pointing to the possible existence of molecular outflows. We fitted and subtracted detected line wings with a single broad Gaussian *before* attempting to analyse the main line. Sixteen sources are found to contain blends of two or more HCO^+ lines, which we attempted to fit with individual Gaussians in order to separate the main line from the blend. Intensities quoted in Table 6 are for the main line only and do *not* contain contributions from line wings or blended lines. The Gaussian fit parameters to the line wings and blended lines are recorded separately in Table 7.

4.2 Mid-infrared associations

We present the association between the maser-selected sample and mid-infrared MSX sources in Table 3. Sixty-eight positions observed have mid-IR emission peaking within $10''$. Of these, 3 are detected at $8\ \mu\text{m}$ but not at $21\ \mu\text{m}$, and 7 are detected at $21\ \mu\text{m}$ but not at $8\ \mu\text{m}$. 15 positions show no evidence of a mid-infrared emission, however 12 of these are identified as MSX ‘dark-clouds’, seen in absorption against the Galactic plane at $8\ \mu\text{m}$. A single source, G30.79+0.20, is detected as a point-source at $21\ \mu\text{m}$ but is embedded within a dark cloud at $8\ \mu\text{m}$.

Of the 80 sources detected in emission or absorption in the mid-IR, 57 have ‘compact’ or unresolved morphologies, 17 are extended and the remainder are confused.

5 DERIVED PHYSICAL PARAMETERS

5.1 Rotational Diagram Analysis

To estimate the temperature and column density of CH_3CN , we have used the rotational diagram (RD) analysis first introduced by Hollis (1982). The method has been developed and expanded on by a number of authors (Loren & Mundy 1984, Turner 1991, Goldsmith & Langer 1999). We provide a brief summary here for convenience.

By solving the radiative transfer equation, assuming low optical depth (i.e. $\tau \ll 1$), we arrive at the well known relation between upper state column density, N_u , and measured line intensity, $\int_{-\infty}^{\infty} T_b dv$

$$N_u = \frac{8\pi k \nu_{ul}^2}{hc^3 A_{ul}} \int_{-\infty}^{\infty} T_b dv, \quad (1)$$

where ν_{ul} is the frequency of the transition in Hz and A_{ul} is the Einstein A coefficient in s^{-1} . Line intensity is in units of K km s^{-1} . All other constants take their usual values in SI units. Assuming local thermal equilibrium (LTE) (i.e. the energy levels are populated according to a Boltzmann distribution characterised by a single temperature, T), the upper state column density is related to the total column density, N , by

$$N_u = \frac{N g_u}{Q(T)} e^{-E_u/kT}, \quad (2)$$

where g_u is the degeneracy of the upper state, E_u is the energy of the upper state in joules and $Q(T)$ is the partition function. Rearranging and taking the natural log of both sides we find

$$\ln\left(\frac{N_u}{g_u}\right) = \ln\left(\frac{N}{Q(T)}\right) - \frac{E_u}{kT}. \quad (3)$$

A straight line fitted to a plot of $\ln(N_u/g_u)$ versus E_u/k will have a slope of $1/T$ and an intercept of $\ln(N/Q(T))$. Temperatures found from this method are referred to as rotational temperatures (T_{rot}) in the literature. In our analysis we used the partition function for CH_3CN quoted in Araya et al. (2005)

$$Q(T) = \frac{3.89 T_{\text{rot}}^{1.5}}{(1 - e^{-524.8/T_{\text{rot}}})^2}. \quad (4)$$

Inherent in the RD method are some formal assumptions which may effect the interpretation of the results. Firstly, the emitting region is assumed to be optically thin. If optical depths are high the measured line intensities will not reflect the column densities of the levels. Optical depth effects will be evident in the rotational diagram as deviations of the intensities from a straight line and a flattening of the slope (Goldsmith & Langer 1999), leading to anomalously large values for T_{rot} .

We have attempted to iteratively correct individual N_u/g_u values by multiplying by the optical depth correction factor, $C_\tau = \tau/(1 - e^{-\tau})$, after the method of Remijan et al. (2004). Assuming Gaussian line profiles, the line-centre optical depth is given by

$$\tau = \frac{c^3 \sqrt{4 \ln 2}}{8\pi \nu^3 \sqrt{\pi} \Delta v} N_u A_{ul} \left(e^{h\nu/kT_{\text{rot}}} - 1 \right), \quad (5)$$

where Δv is the FWHM of the line profile in km s^{-1} (see Goldsmith & Langer (1999) and Remijan et al. (2004) for a formal description). In our calculations we initially assumed the source fills the beam. We find that the corrected optical depth is always $\ll 1$, even in the $K=0$ transitions, and the correction factors are less than 1%. The FWHM Mopra beam at 92 GHz

is $\sim 36''$. If previous high-resolution surveys (e.g. Remijan et al. 2004, Wilner, Wright & Plambeck 1994) are indicative, the angular size of CH_3CN emission will be $< 10''$. Our measurements of CH_3CN intensity are thus likely to be affected by a dilution factor of > 13 and the measured optical depth, and therefore the correction factors, are anomalously low because of this.

If we then assume a $7''$ source size and determine the correction factor, we find that the rotational temperature is corrected down by $\sim 10\%$ and the total column density is corrected up by $\sim 6\%$, on average. In their analysis of Sagittarius B2 Nummelin et al. (2000) chose a source size which minimises the χ^2 value on their RD fits. They find that for some molecules the best fit to the data is obtained for beam filling factors $\ll 1$. We find that in most cases the quality of our fits *deteriorate* as the beam filling factor is decreased, most likely because our fits are not well constrained due to low signal/noise data. Thus we use a beam filling factor of 1 in our final calculations, and beam-averaged column densities stemming from this analysis should be considered a lower limit.

Secondly, the emitting region is assumed to be in LTE where the population within a K ladder is characterised by a single excitation temperature, described by a Boltzmann distribution. For the non-LTE case the temperature and column density will be underestimated.

Figure 4 shows a typical example of a rotational diagram made using the $J=6-5$ and $J=5-4$ transitions. Calibration errors between the J transitions are approximately 30% and manifest themselves as a vertical offset between the two sets of points in the graph. The change in the FWHM of the Mopra beam between 92 and 110 GHz has been measured by Ladd et al. (2005), and the intensities of the $J=6-5$ lines have been divided by the relative beam filling factor, given by $(\theta_{110\text{ GHz}}/\theta_{93\text{ GHz}})^2 = (34''/36'')^2$. As the K components within a single J transition were observed simultaneously, the relative errors are smaller and arise from the quality of the detection and stability of the bandpass. Error bars mark the 1σ error in the column density of individual K components, as determined by Gaussian fitting. In the analysis we fit the $J=6-5$ and $J=5-4$ data separately, shown in Figure 4 as dashed lines. We took as our final result the weighted average of the derived T_{rot} and N, plotted on the diagram as a solid line. The rotational diagrams for the remaining sources are available in the online edition of this paper.

The results of our rotational diagram analysis are presented in Table 8. In general, the observed intensities were well fit by a straight line, except for G10.47+0.03 which exhibited anomalous line ratios and for which a meaningful temperature could not be derived. Rotational temperatures range from 28 K to 166 K with an average value of 57 K. Temperatures derived from sources where we detected less than four CH_3CN K components are not well constrained, but are still useful for comparative purposes.

We compared distributions of T_{rot} for UHCn regions and isolated masers, but a KS-test did not find any significant difference in rotational temperature between them.

It is interesting to compare our derived rotational temperatures and column densities to previously published results. Eleven sources reported here overlap with previous studies by Pankonin et al. (2001), Hatchell et al. (1998), Olmi, Cesaroni & Walmsley (1993) and Churchwell, Walmsley & Wood (1992). Table 9 is a reproduction of Table 6 from Pankonin et al. (2001), expanded to include this paper. In it we compare values of derived rotational temperature and column density. Our values for T_{rot} are generally lower, typically by a factor of ~ 2 , except when compared to values

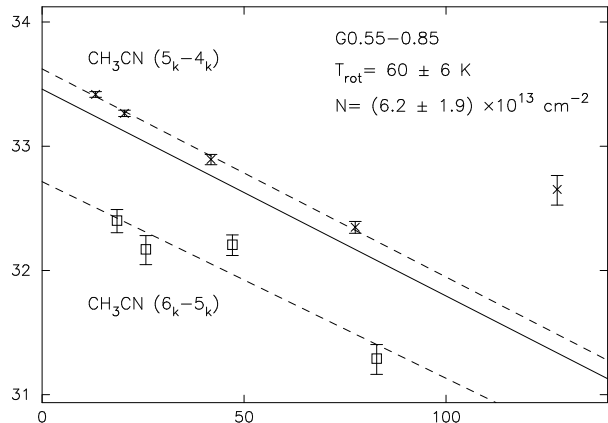


Figure 4. CH_3CN rotational diagram of $\ln(N_u/g_u)$ vs E_u/k for the source G0.55–0.85. The $J=5-4$ K-components are plotted with crosses and the $J=6-5$ K-components are plotted with squares. Error bars denote the 1σ errors in the Gaussian fit to individual lines. The rotational temperature, T_{rot} , and total column density, N, may be found from the slope and y-axis intercept of a straight line fit to the data points. We fit the K-ladders separately (dashed lines) and in most cases took the weighted mean of the results as our final values for T_{rot} and N (solid line). The error in T_{rot} is dependant only on the relative calibration between lines in a single spectrum. The error in N is dependant on the absolute calibration, and is approximately 30%.

derived by Olmi et al. (1993), who also employ the CH_3CN (5–4) transition in their analysis. The other studies have included data from the $J=12-11$ transitions or higher. The $J=5-4$ and $J=6-5$ transitions have upper-state energies spanning $\sim 8-130$ K compared to $\sim 68-500$ K for the $J=12-11$ transition. It is likely our survey is sensitive to cooler gas, as evidenced by our lower derived temperatures, whereas the surveys utilising higher energy transitions in their analysis are sensitive to hotter gas. These assertions are supported by recent observations by Araya et al. (2005) who found it necessary to fit two temperatures to their observations of the $J=5-4$, $6-5$, $8-7$ and $12-11$ transitions of CH_3CN . The lower energy lines yield typical temperatures of 35 K whereas the higher energy lines are well fit by temperatures above 90 K, suggesting the existence of a hot molecular clump embedded in a cooler envelope, or simply a temperature gradient. Further evidence of a temperature gradient in hot cores is presented by Olmi et al. (2003), who observed CH_3CN (6–5) in G29.96–0.02. An analysis of the angular diameter of the emission measured in each K component shows that higher energy transitions are excited closer to the centre of the hot core.

Column densities derived here are comparable to those reported in other work. They are higher by factors of $\sim 1.5-2$ compared to the work of Pankonin et al. (2001), but significantly lower than earlier surveys by Olmi, Cesaroni & Walmsley (1993) and Churchwell, Walmsley & Wood (1992). Caution is needed, however, in making a direct comparison of column-densities between surveys, as the beam-sizes and excitation conditions of different observations are not well matched. There is also confusion in the literature with regard to the correct partition function for CH_3CN , which may lead to the column-densities being miscalculated by as much as a factor of 5 (Araya et al. 2005). The high figures derived in this paper compared to Pankonin et al. (2001) probably reflect the greater volume of lower temperature gas probed by the $36''$ Mopra beam compared to more compact, warmer gas probed by other surveys.

5.2 HCO⁺ Column Density and Abundance

We derive HCO⁺ column densities assuming optically thick HCO⁺ and optically thin H¹³CO⁺ lines.

The expression for the measured brightness temperature, T_b, of a molecular transition is:

$$\frac{T_b}{\eta_{bf}} = T_r = [J_\nu(T_s) - J_\nu(T_{bg})](1 - e^{-\tau}), \quad (6)$$

where

$$J_\nu(T) = \frac{h\nu_u}{k} \frac{1}{(e^{h\nu_u/kT} - 1)}, \quad (7)$$

and where T_s is the temperature of the source, T_{bg} is the temperature of the background radiation (2.73 K), τ is peak optical depth, and η_{bf} is the beam filling factor, given by Ω_s/Ω_b. Assuming the HCO⁺ line is optically thick, (1 - e^{-τ} ≈ 1), we can calculate an excitation temperature according to

$$T_{ex} = T_s = \frac{h\nu_u}{k} \left[\ln \left(1 + \frac{(h\nu_u/k)}{T_{thick} + J_\nu(T_{bg})} \right) \right]^{-1}, \quad (8)$$

where T_{thick} = T_r is the beam corrected brightness temperature of the HCO⁺ line. We assume the HCO⁺ and H¹³CO⁺ emission arises from the same gas and shares a common excitation temperature. Given a known excitation temperature, the optical depth of the H¹³CO⁺ line may be found from

$$\tau_{thin} = -\ln \left[1 - \frac{T_{thin}}{[T_{ex} - J_\nu(T_{bg})]} \right], \quad (9)$$

where T_{thin} = T_r is the beam corrected brightness temperature of the H¹³CO⁺ line.

Equations 2 and 5 may then be applied to find the total H¹³CO⁺ column density, again assuming LTE conditions. The partition function for linear rotors is well approximated by Q(T) = (kT_{ex})/(hB), where B is the rotational constant in Hz (43377 MHz for H¹³CO⁺). The HCO⁺ and H¹³CO⁺ column densities are related through their relative abundance ratio,

$$X = \frac{[HCO^+]}{[H^{13}CO^+]} = \frac{N_{HCO^+}}{N_{H^{13}CO^+}}, \quad (10)$$

which is partially dependant on the fraction of ¹³C present in the interstellar medium. A Galactic gradient in the ¹²C/¹³C ratio, ranging from ~20 to ~70, has been measured using several methods (see Savage et al. (2002) and references therein). The measurement uncertainties are large, however, and the ratio of [HCO⁺]/[H¹³CO⁺] may also be affected by chemistry. Thus, we have assumed a constant X = 50 for all our calculations.

A major source of error in this analysis stems from the assumption that the HCO⁺ lines provide a meaningful estimate of the excitation temperature. In many cases the line profiles show evidence of self absorption and are poorly fit by simple Gaussians. As outlined in § 3.1 we used two methods to estimate the HCO⁺ brightness temperature. In the first method we measure the brightness temperature from a Gaussian fit to the profile, by masking off the absorption dip. In the second method we took as the value for brightness temperature the highest peak in the profile (see Figure 3). If the emission is smaller than the beam, the filling factor, η_{bf}, will be less than one and the excitation temperature will be underestimated. Using the above methods we find average excitation temperatures of ~7.5 K and ~6.1 K, respectively. These values are considerably lower than the ~15 K temperatures quoted in previous work (e.g. Girart et al. 2000) and we conclude that the

emission is beam diluted in a significant fraction of our observations. In our final analysis we have assumed an excitation temperature of 15 K and the column densities are calculated solely from the H¹³CO⁺ lines. The H¹³CO⁺ lines were well fit with Gaussians and are consistent with being optically thin in most cases. The results of the analysis are presented in Table 10. As the source size is unknown the values quoted are beam-averaged, assuming a filling factor of one.

6 ANALYSIS & DISCUSSION

We detect CH₃CN towards all classes of sources: UCH II regions, isolated masers and maserless cores. This result confirms a direct link between each of these objects and massive star formation. In the following analysis we will discuss the implications for a possible evolutionary sequence.

6.1 The presence of an UCH II region

The CH₃CN detection rate towards maser-sources associated with an UCH II region (radio-loud), compared to isolated maser sources (radio-quiet) is strikingly different.

Figure 5-A shows the distributions of integrated CH₃CN (5–4) intensity for the two classes of source, including non-detections, which are summed in the shaded bar. CH₃CN was detected towards 18 out of the 19 radio-loud sources (95 %) compared to only 40 out of 64 radio-quiet sources (63 %). Furthermore, the average integrated CH₃CN (5–4) intensity measured towards the radio-loud sources is 7.4 K km s⁻¹, stronger than the average measured towards the radio-quiet sources, which is 3.5 K km s⁻¹. We used a Kolmogorov-Smirnov (KS) test to measure the difference between the distributions of the two classes. Non-detections are included as upper limits, measured from the RMS noise in the spectra, and by assuming K=0 and K=1 CH₃CN components of linewidth 4 km s⁻¹ are present at a 3σ level. Using this conservative estimate a KS-test indicates there is only a 0.13 % probability of the samples being drawn from the same population. Probabilities below ~1 % indicate that the distributions are significantly different.

A similar result applies for H¹³CO⁺. Figure 5-B shows the distributions of H¹³CO⁺ intensity for the two classes of objects. The mean intensity for the radio-loud sources is 4.3 K km s⁻¹ compared to 1.9 K km s⁻¹ for the radio-quiet sources. A KS-test returns a probability of 0.02 % that the distributions are similar.

We find the HCO⁺ lines are also brighter towards radio-loud sources, however we do not consider them in this analysis as they show evidence of optical depth effects which may confuse their interpretation.

6.1.1 The effect of distance on the results

A higher CH₃CN detection rate towards UCH II regions is consistent with a fall-off in flux with distance in the original radio survey. Our classification of sources into radio-loud and radio-quiet regions may be artificial, and undetected UCH II regions may simply be a result of the sources being further away. Closer examination shows this not to be the case. The distribution of distances to the two populations is shown in Figure 6. No UCH II regions have been detected further than 9 kpc away, however only 9 out of 83 sources lie at greater distances. A comparison yields an 53 % probability that the

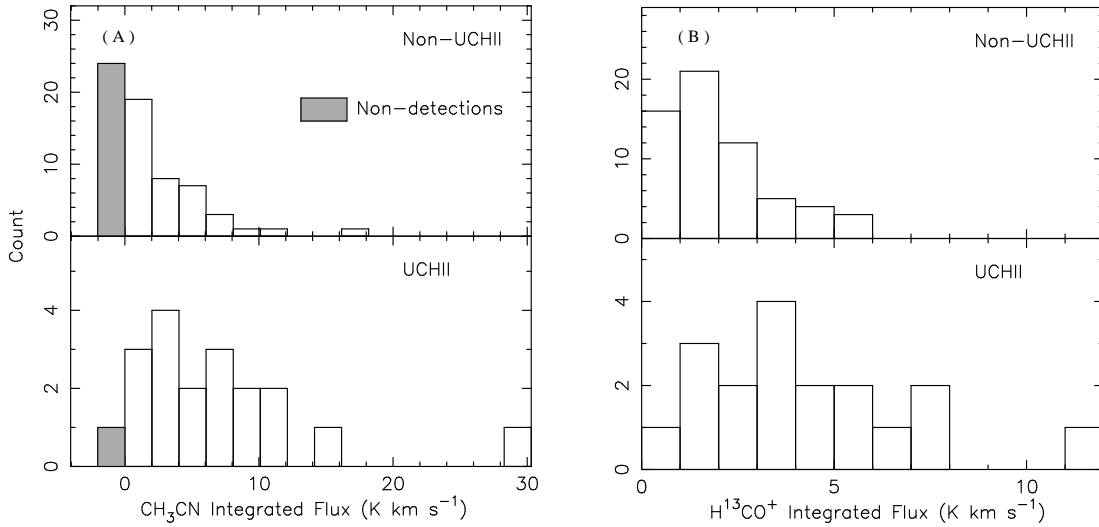


Figure 5. **A)** Distributions of integrated CH_3CN (5–4) flux, summed over all detected K-components, for sources with UCHII regions within the Mopra beam (bottom) and those without (top). The shaded bar represents the number of CH_3CN non-detections for each population. A KS-test yields a maximum difference of 0.48 between the distributions, with a probability of 0.13 % of being drawn from the same parent distribution. **B)** Distributions of integrated H^{13}CO^+ (1–0) flux for the same populations. Lines associated with UCHII regions are markedly brighter than those without. A KS-test yields a difference of 0.55 between the distributions, with an associated probability of 0.02 % of being drawn from the same parent distribution. A similar result has been found for the HCO^+ lines.

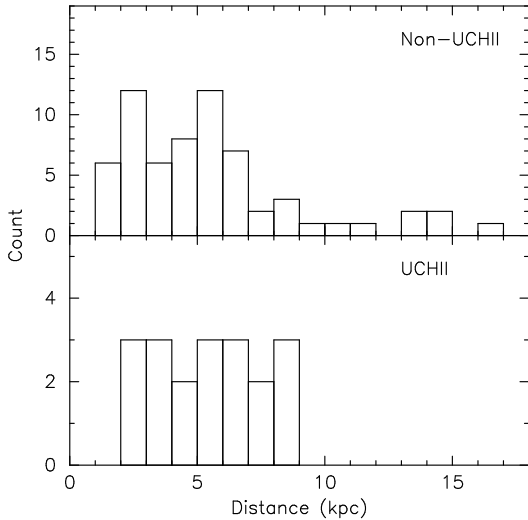


Figure 6. Distributions of distances in kiloparsecs for sources with and without associated UCHII regions. A KS-test yields a probability of 53 % that samples are consistent with being drawn from the same population and thus probe the same distances.

classes are consistent with being drawn from the same population and thus probe the same distance range.

We further examine the detection limits on the Walsh et al. (1998) 8.64 GHz radio survey from which our sample was drawn. The quoted 1σ sensitivity is ~ 1 mJy. Assuming a 3σ detection, the limiting distance, D , in kpc at which free-free radio emission from a UCHII region is detectable, may be calculated from Kurtz, Churchwell & Wood (1994):

$$\left(\frac{S_\nu}{\text{Jy}}\right) = 1.32 \times 10^{-49} N_L \left(\frac{D}{\text{kpc}}\right)^{-2} a(\nu, T_e) \left(\frac{\nu}{\text{GHz}}\right)^{-0.1} \left(\frac{T_e}{\text{K}}\right) \quad (11)$$

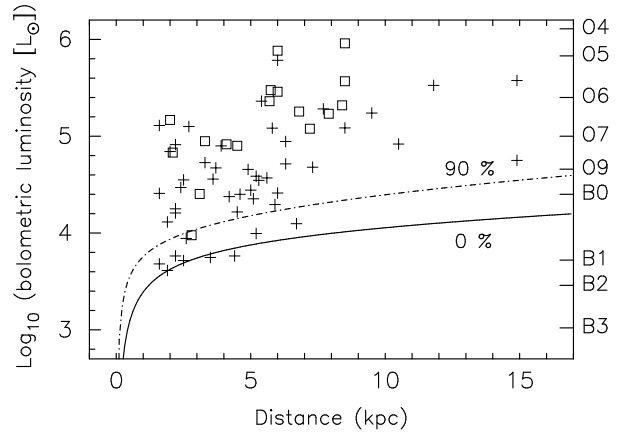


Figure 7. A plot of distance versus bolometric luminosity for the sample. The solid line shows the 3σ detection limit for 8.67 GHz radio continuum emission, assuming all the Lyman-continuum flux contributes to creating an UCHII region. The dashed line shows how the detection limit changes if 90 % of the ionising photons are absorbed by dust. UCHII regions are represented by squares, and isolated maser sources by crosses.

where $\nu = 8.64$ GHz is the frequency, $T_e \approx 10^4$ K is the electron temperature, $a(\nu, T_e)$ is a factor of order unity tabulated by Mezger & Henderson (1967) and N_L is the number of Lyman-continuum photons. Values of N_L for early-type stars are tabulated by Panagia (1973), however, in practise some fraction of the emitted ionising photons will be absorbed by dust before ionising the surrounding medium. In a study of UCHII regions, Kurtz et al. (1994) found that between 50 % and 90 % of the ionising photons are absorbed for the majority of their sample. Figure 7 is a plot of luminosity against distance, in kpc, for all the sources whose luminosity could be determined. The solid line marks the 3σ sensitivity limit to 8.64 GHz radio continuum, assuming no Lyman-continuum photons are absorbed, while the dotted line shows the sensitivity

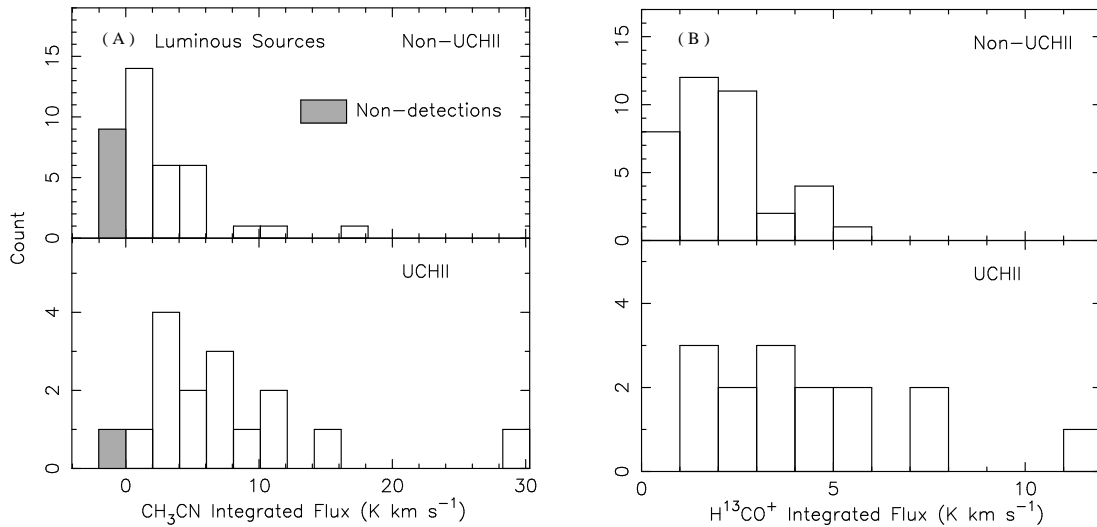


Figure 8. As for Figure 5 but limited to sources which are luminous enough to have detectable UCHII regions, assuming no less than 90 % of the ionising photons are attenuated. **A)** A KS-test yields a maximum difference of 0.50 between the CH_3CN distributions, with an associated probability of 0.93 % of being drawn from the same parent distribution. **B)** Similarly the maximum difference between the H^{13}CO^+ populations is 0.56, with an associated probability of 0.12 %.

limit assuming 90 % of all ionising photons are absorbed. The luminosities of our sources were determined by fitting a 2-component greybody to available MSX, SCUBA, and IRAS fluxes as discussed earlier and are accurate to a factor of ~ 2 . For those sources above the 90 % absorption limit, UCHII regions would have been detected if they existed, and it is most unlikely that the comparison between CH_3CN detected for UCHII regions and isolated maser sources is biased. We plot Figure 8-A as per Figure 5, but include only sources luminous enough to have detectable radio-continuum emission, assuming 90 % attenuation of ionising photons. We find that the CH_3CN distributions are still significantly different, with only a 0.9 % probability of being drawn from the same population. The H^{13}CO^+ intensity distribution for the two classes, filtered to the same luminosity limit, is shown in Figure 8-B. A KS-test returns a 0.1 % probability of them being drawn from the same population.

The apparent enhancement in *line brightness* towards UCHII regions could be mimicked by the effect of beam dilution. A previous high resolution survey for CH_3CN has found the typical size of the emitting region to be $< 10''$ (Remijan et al. 2004). Assuming a constant spatial size, the effect of beam dilution on the CH_3CN brightness temperature will depend on the angular size and hence distance to the source. We have shown that the radio-loud and radio-quiet samples probe the same distance range and thus neither class is biased towards being nearer.

Figure 9 plots measured CH_3CN (5–4) flux against kinematic distance and we do not find any correlation. As an additional test we can recover the line-luminosity by multiplying by the square of the distance. This has the effect of increasing the spread in the brightness distribution for both samples, however a KS-test returns a 1.5 % probability in the case of CH_3CN and a 1.0 % probability in the case of H^{13}CO^+ that the radio-quiet and radio loud line-luminosity distributions are drawn from the same population. The average line-luminosity remain higher for the radio-loud class of objects.

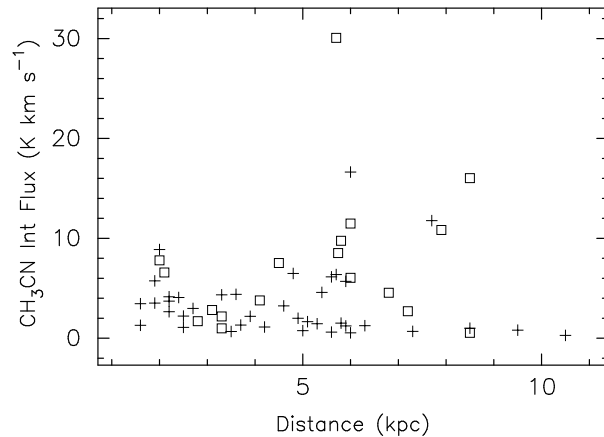


Figure 9. Plot of integrated CH_3CN (5–4) flux vs kinematic distance, in kpc. UCHII regions are marked with squares and isolated maser sources are marked with crosses. No correlation is evident.

6.1.2 Interpretation.

Previous work on hot cores suggests CH_3CN is the tracer of choice for massive protostars in the hot core phase (e.g. Kurtz et al. 2000), however we find CH_3CN is preferentially associated with UCHII regions. Pankonin et al. (2001) conducted a CH_3CN (12–11) survey for hot cores and also found a correlation between the presence of CH_3CN and UCHII regions. In one of the few high resolution studies Remijan et al. (2004) used the BIMA array to image the hot core regions W51e1 and W51e2 and found that the CH_3CN emission was centred on known UCHII regions.

That we detect CH_3CN towards isolated methanol masers, for which there are no other tracers indicative of star-formation, clearly suggests that these objects are internally heated. The lack of CH_3CN towards some isolated maser sources is consistent with them being at a less advanced stage of evolution compared to UCHII regions. In young hot cores we would expect any emission to be concentrated in the central regions, where the protostar has heated

the dust sufficiently for icy mantles to evaporate and for CH_3CN to form. As the temperature rises icy mantles continue to evaporate and the emitting region expands outwards and becomes easier to detect. UCH_{II} regions represent the most advanced evolutionary stage before the young star emerges from its natal cocoon. It is reasonable to assume a relatively extended envelope of CH_3CN may exist around the UCH_{II} region, which is less beam diluted and easier for a single-dish survey to detect. Such a scenario is lent weight by high resolutions ($\sim 1''$) observations of the hot core in G29.96–0.02. Olmi et al. (2003) derive a kinetic temperature of ~ 150 K from vibrationally excited CH_3CN , significantly higher than the ~ 90 K found by Pratap et al. (1999), using ground state lines. Olmi et al. (2003) also find evidence for a temperature gradient, as the emission from higher energy transitions is confined to increasingly compact regions.

Alternatively, the dominant CH_3CN emission may emanate from an unresolved hot core within the same beam. G29.96–0.02 is the classic example of a hot core on the edge of a cometary UCH_{II} region (c.f. Cesaroni et al. 1998). We note that in the present survey the CH_3CN emission is classified as being associated with the UCH_{II} region, as at 3-mm wavelengths, Mopra does not have the resolution to disentangle the hot core from the nearby ($\sim 5''$) radio emission. Conclusions drawn from this work refer to the properties of “clumps”, which are may contain more than one core. We speculate that clumps containing UCH_{II} regions are more likely to contain an evolved hot core and thus have greater abundances of daughter species, like CH_3CN .

Further enhancements come from the work of Mackay (1999) who developed a chemical model of the hot core G34.3+0.15. The model predicts an enhanced abundance of CH_3CN in the presence of a far-ultraviolet radiation field. MacKay assumed a spherically symmetric core surrounded by a photon dissociation region (PDR), created by the ultraviolet radiation from a nearby OB association. It is more likely that the cores are inhomogeneous and have clumpy density distributions, in which case the incident radiation will penetrate deeper and the CH_3CN abundance will be further enhanced. Seven out of the nineteen UCH_{II} regions in our sample are exactly coincident with methanol maser sites, however the remaining twelve are offset by less than a beam and it is likely that these sources have a complex clumpy structure.

6.2 V_{LSR} and Linewidths

The difference between the CH_3CN and H^{13}CO^+ V_{LSR} is plotted in Figure 10. The velocity offsets are all less than 2 km s^{-1} , indicating that the molecules are probably within the same star forming region. 92% of the sources have velocity offsets less than the fitting errors ($\pm 0.4 \text{ km s}^{-1}$), suggesting that they trace the same clump or core within the beam.

Figure 11 displays the distributions of linewidth from the Gaussian fits to the CH_3CN and H^{13}CO^+ lines. Both distributions are roughly symmetrical about means of 4.9 and 3.5 km s^{-1} respectively, higher than typical linewidths of $< 2 \text{ km s}^{-1}$ measured in low-mass star-forming regions. At 100 K the thermal linewidths of $\text{CH}_3\text{CN}(5-4)$ and $\text{H}^{13}\text{CO}^+(1-0)$ are 0.20 km s^{-1} and 0.24 km s^{-1} respectively, with turbulence or bulk gas motions accounting for most of the broadening. The CH_3CN linewidth is broader than the H^{13}CO^+ linewidth, which suggests that the two species trace different spatial scales. This is consistent with CH_3CN being concentrated around a dynamic core and the H^{13}CO^+ tracing a more extended quiescent envelope.

We also note that sources with associated radio contin-

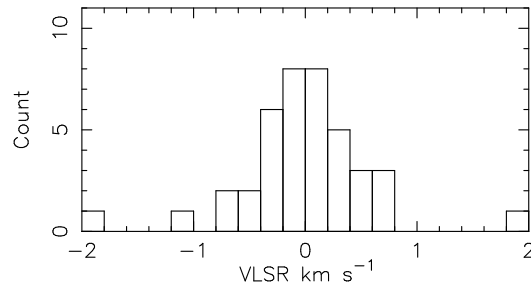


Figure 10. $V_{\text{LSR}}(\text{CH}_3\text{CN} - \text{H}^{13}\text{CO}^+)$. The difference in velocity between the CH_3CN and H^{13}CO^+ lines is within the errors, making it likely that the emission arises from the same source. Velocity errors are derived from Gaussian fits and are typically $\pm 0.4 \text{ km s}^{-1}$.

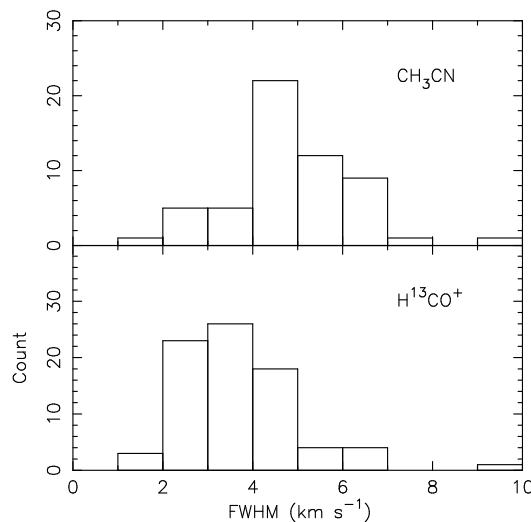


Figure 11. $\text{CH}_3\text{CN}(5-4)$ (top panel) and $\text{H}^{13}\text{CO}^+(1-0)$ (bottom panel) linewidth distributions. Both distributions are roughly symmetrical about means of 4.9 and 3.5 km s^{-1} respectively.

uum emission have larger linewidths than sources without (i.e. isolated maser sources). The mean $\text{CH}_3\text{CN}(5-4)$ linewidths are 6.2 km s^{-1} for UCH_{II} regions versus 4.7 km s^{-1} for isolated masers, while the mean $\text{H}^{13}\text{CO}^+(1-0)$ linewidths are 4.0 km s^{-1} for UCH_{II} regions versus 3.4 km s^{-1} for isolated masers. Linewidths are a rough indicator of star-formation activity: we expect to see greater linewidths towards more dynamic regions. The greater linewidths reported for UCH_{II} regions are certainly consistent with a scenario where the isolated maser sources are precursors to the UCH_{II} phase.

6.3 HCO^+ Line Profiles

Almost all HCO^+ lines exhibit asymmetric line profiles or high-velocity line wings. Complex profiles may be interpreted as either multiple emitting regions along the same line of sight, or as a single emitting region with cold absorbing gas intervening. By examining the line profiles of optically thin H^{13}CO^+ we attempt to distinguish between these two causes, and find that most sources are composed of a single broad line with a self absorption dip. Depending on the shape of the profile, we can infer inward or outward motions. Blue-skewed profiles are predicted by collapse models of star formation, however, rotation or outflow-blobs can

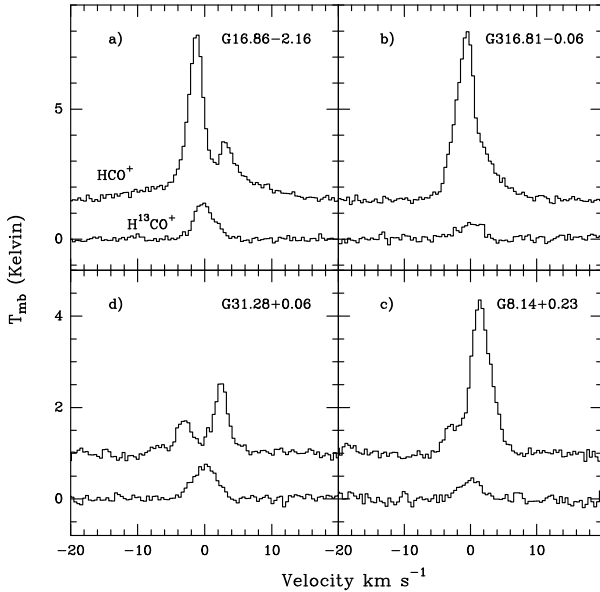


Figure 12. Example HCO^+ line profiles. **a)** Blue double-peaked profile, **b)** blue skewed profile, **c)** red skewed profile, **d)** red double-peaked profile.

also produce similar line shapes. The presence of a statistical excess of blue profiles in a survey can indicate that inflow is a likely explanation (Wu & Evans 2003). Two methods of characterising line profiles appear in the literature. Where the opacity is high and the line takes on a double-peaked form, Wu & Evans (2003) measure the ratio of the blue to the red peak $[T_{\text{MB}}(\text{B})/T_{\text{MB}}(\text{R})]$. A blue profile fulfils the criterion: $[T_{\text{MB}}(\text{B})/T_{\text{MB}}(\text{R})] > 1$ by a statistically significant amount. At lower optical depths the absorption will be less severe and the line will appear as a skewed peak with a red or blue shoulder. Mardones et al. (1997) suggest an alternative measurement: the line may be classed as blue if the difference between the peak velocity of the optically-thick and optically-thin lines is greater than 1/4 the line width of the optically thin line: $\delta v = (v_{\text{thick}} - v_{\text{thin}})/v_{\text{thin}} < -0.25$. Similarly for a red profile: $\delta v = (v_{\text{thick}} - v_{\text{thin}})/v_{\text{thin}} > 0.25$. Figure 12 displays a range of HCO^+ profiles from blue to red. We have classed all detected HCO^+ lines using one of the two schemes above. The results are displayed in Figure 13. We identify 9 blue and 8 red profiles using the δv measurement, and 12 blue and 10 red profiles using the brightness method. To effect a comparison with other surveys we adopt the concept of “excess” introduced by Mardones et al. (1997) and later used by Wu & Evans (2003): $E = (N_{\text{blue}} - N_{\text{red}})/N_{\text{total}}$, where N_{total} is the number of sources in the sample. The excesses using the δv and brightness methods are $E = 0.02$ and 0.08 , respectively. In comparison Wu & Evans (2003) measure excesses of 0.29 and 0.21 in a sample of 28 low-mass star-forming regions.

We also split our sample into radio-strong and radio-weak population, searching for differences in the incidence of blue or red profiles; however we do not find any convincing difference between the populations.

6.4 MSX colours

The MSX colours of our sample are primarily determined by the temperature and optical depth of the dust in which they are embedded. As a first attempt to distinguish between classes of source we

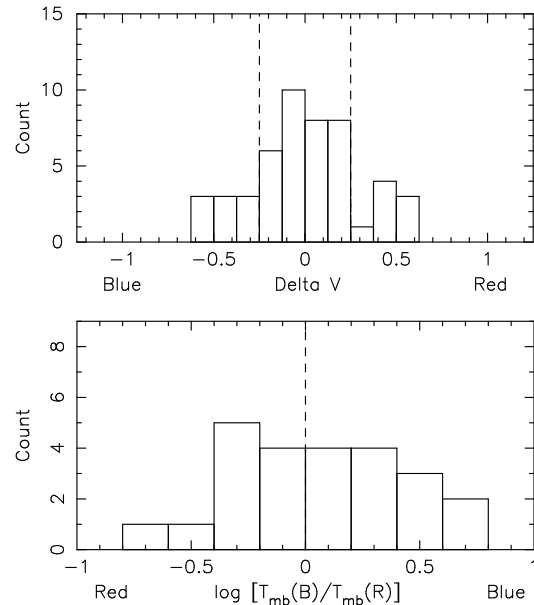


Figure 13. Distributions of red and blue profiles measured by $(v_{\text{thick}} - v_{\text{thin}})/v_{\text{thin}}$ (upper panel) and $[T_{\text{MB}}(\text{B})/T_{\text{MB}}(\text{R})]$ (lower panel). In the top panel the vertical dashed lines mark the absolute velocity difference beyond which profiles are considered to be blue or red skewed. In the lower panel the line divides red and blue profiles. One red and one blue source were discarded as the difference in peak height was within the 1σ noise on the spectrum.

have derived the colour temperature from the $21/14\ \mu\text{m}$ ratio, assuming blackbody emission. Larger ratios are equivalent to lower temperatures and increasingly reddened colours. We have avoided using the $21/8\ \mu\text{m}$ or $21/12\ \mu\text{m}$ ratios because of possible contamination from PAHs emission at 7.7 , 8.6 and $13.3\ \mu\text{m}$, and silicate features at 9.7 and $11.3\ \mu\text{m}$. Distributions of derived temperatures for sources split into classes with and without UCHII regions and CH_3CN emission are displayed in Figure 14. A KS-test fails to find any significant difference between the classes.

Figure 15 shows a plot of colour temperature against T_{rot} , however no correlation is evident, most likely because the thermal infrared and CH_3CN emission arise in different regions. Although optical depth effects render colour ratios a poor indicator of kinetic temperature, we note that the rotational temperatures are on average three times lower than the colour temperatures.

Lumsden et al. (2002) have made a study of sources in the MSX catalogue in an effort to perform a census of massive protostars in the Galactic plane. They have arrived at a set of mid-infrared colour criteria forming the first step in a selection process designed to find the majority of massive protostars present in the Galaxy. As most massive protostars have a featureless red continuum rising between 1 and $100\ \mu\text{m}$, they require that $F_8 < F_{14} < F_{21}$. Known massive protostars, when plotted on a mid-infrared colour-colour diagram, have an infrared excess such that $F_{21}/F_8 > 2$. In the absence of other selection criteria, sources which satisfy these colour-cuts will include massive protostars, evolved stars, planetary nebula and UCHII regions. Applying these criteria to our data-set we initially discard 28 sources which have incomplete data. Figure 16 shows the mid-infrared colour-colour diagrams for the remaining 55 sources. Associations with UCHII regions and CH_3CN are noted by way of different symbols and the selection limits are marked as horizontal and vertical dashed

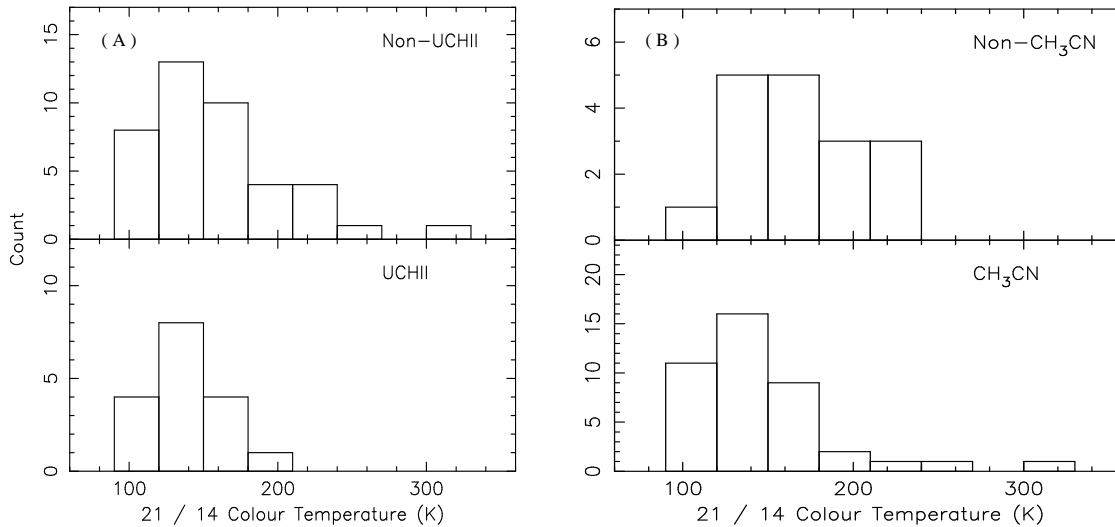


Figure 14. Colour temperatures derived from the 21/14 μm ratio, for sources with and without associated UCHII regions, (A), and CH_3CN emission, (B). A KS-test cannot distinguish between the distributions with confidence.

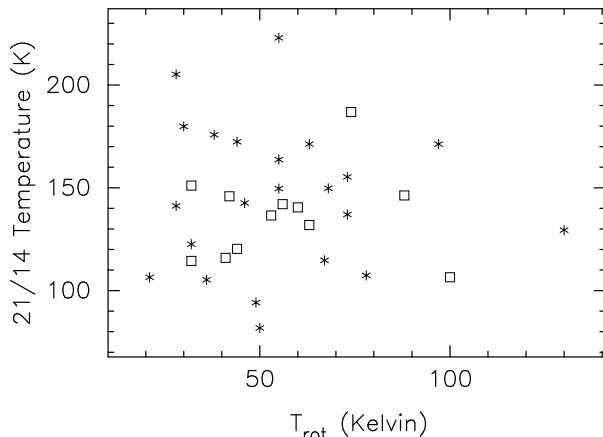


Figure 15. 21/14 μm ratio vs T_{rot} . Squares represent sources containing UCHII regions. The 21/14 μm ratio does not appear to be correlated with the temperature obtained from the rotational analysis of the CH_3CN . Note also that the distribution of T_{rot} is identical for the UCHII regions and isolated masers.

lines. Five sources fail the selection criteria: G23.26–0.24 fails both colour-cuts, G30.90+0.16 fails because $F_{21}/F_8 < 2$ and the remaining three (G6.54–0.11, G12.72–0.22, G16.59–0.05) fail because $F_{14} < F_8$. All sources are radio-quiet and three have detected CH_3CN emission, but are unremarkable in other ways. No clustering is seen on the colour-colour plots that would distinguish the classes of source, except perhaps a slight enhancement of the 14/12 μm ratio for UCHII regions. UCHII regions are on average also a factor of two brighter in all bands than radio-quiet sources. To further separate young massive stars from planetary nebula and evolved stars Lumsden et al. (2002) resorted to near-infrared JHK colour selection criteria. 6.7 GHz methanol-masers have not, to date, been found towards low-mass star forming regions and we believe that all of our maser sources represent massive stars (Minier et al. 2005).

Potentially the most interesting sources are ‘MSX-dark clouds’, seen in absorption against the Galactic plane, and the

‘MSX-red’ sources, detected only at 21 μm . It has been suggested that these sources harbour massive protostars at earlier, more obscured phases of massive star-formation, characterised by low temperatures ($T \sim 30$ K) and spectral energy distributions which peak in the sub-millimetre and far-infrared. Table 11 summarises the properties of the sources which fall into these categories. The ‘MSX-dark’ category contains thirteen sources, one of which (G30.71–0.06) is within 30'' of a UCHII region. The ‘MSX-red’ category contains seven sources, one of which (G30.79+0.20) is also seen in absorption at 8 μm but is detected in emission at 21 μm .

We find that the ‘MSX-red’ sources are indistinguishable from the bulk of the sample, having approximately the same molecular detection rates and brightness. Four out of eight sources exhibit asymmetric HCO^+ profiles, three of which are skewed to the red, suggestive of outflowing motions.

‘MSX-dark’ sources exhibit distinct differences from the bulk of the sample. 91% were detected in CH_3CN , and the CH_3CN and H^{13}CO^+ brightness temperatures tend to be higher. However, by their nature dark-clouds are located nearby making it easier to detect weak lines. Seven of twelve sources exhibit asymmetric HCO^+ profiles, six of which are skewed to the blue, indicative of in-falling motions, and consistent with a scenario of cloud collapse. Further analysis is required to judge if these cores will collapse to form massive stars.

6.5 Maserless Sources

Six maserless sources, identified by thermal emission at 1.2-mm from the work of Hill et al. (2005), were included in the source list as potential precursors to the hot core phase. One of these, G5.89–0.39, was subsequently identified as an UCHII region. The remaining five are spread among the classes of source identified in previous section: G0.26+0.01 and G14.99–0.70 are MSX-dark clouds, G5.90–0.44 and G12.72–0.22 are bright and partially resolved MSX sources, and G15.03–0.71 is embedded in confused region of extended emission near the M17 molecular cloud. All lie at distances nearer than 4 kpc, except for G0.26+0.01 which we place at the distance of the Galactic centre. CH_3CN is moderately detected towards all sources, except G15.03-

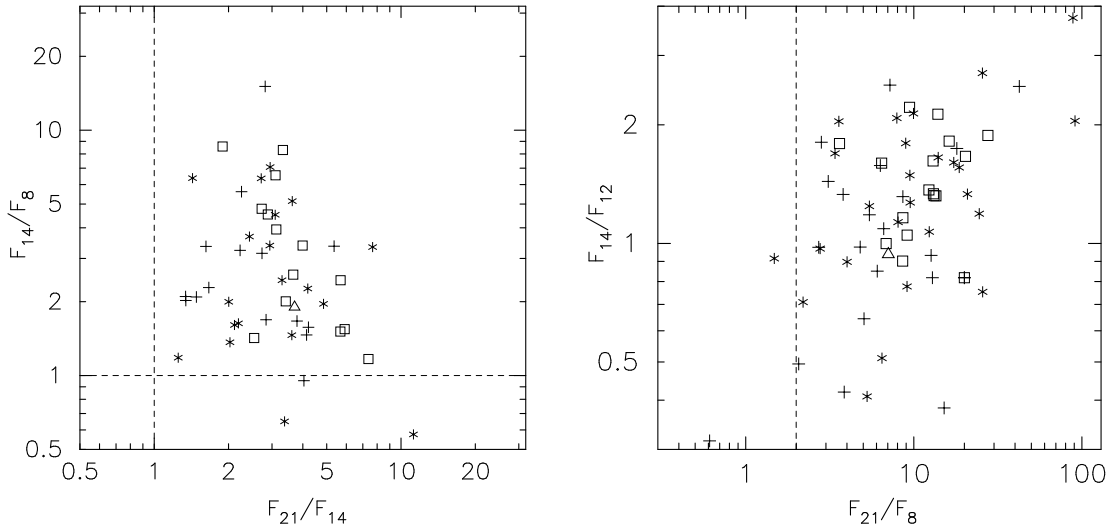


Figure 16. Mid-infrared colour-colour diagrams for sources detected in all bands. The following symbols mark classes of source: Square = UCHII region with CH_3CN , Triangle = UCHII without CH_3CN , Star = Non-UCHII region with CH_3CN , Cross = Non-UCHII region without CH_3CN . The dashed lines mark the selection criteria proposed by Lumsden et al. (2002): $F_8 < F_{14} < F_{21}$ and $F_{21}/F_8 < 2$. Sources which fulfil these criteria include MYSOs, UCHII regions, evolved stars and planetary nebula.

0.71. HCO^+ and H^{13}CO^+ are found towards all sources while the H^{13}CO^+ linewidths vary from 2–4.5 km s^{-1} without any obvious relation to MSX brightness or class. The absence of a further link between these maserless sources and the spread in observed properties suggests a range of evolutionary phases; i.e. the absence of maser emission towards these sources does not necessarily indicate an early phase star-formation, even with the presence of CH_3CN .

7 SUMMARY & CONCLUSIONS

We have detected 58 candidate hot molecular cores through the presence of CH_3CN emission from a sample of 83 methanol maser selected star-forming regions, including 43 new detections. All sites are associated with mm-continuum thermal emission, seen at 1.2-mm, 450 μm and 850 μm . Six sites are not directly associated with maser emission but are within the same star-forming region. Our major findings are as follows:

(i) CH_3CN is commonly detected towards methanol maser sites, but is more prevalent and brighter in the presence of a UCHII region, independent of the distance to the source.

(ii) CH_3CN is detected towards isolated methanol maser sites, where no nearby external heating sources exist. This strongly suggests that these sources are internally heated. Conversely, the lack of CH_3CN towards some isolated maser sites is consistent with them being at a less advanced stage of evolution than UCHII regions.

(iii) We report the CH_3CN rotational temperatures for 38 sources where at least three K components were detected. Values range from 28 to 166 K. These values are generally lower than those found in previous studies utilising higher energy transitions. Derived column densities are poorly constrained but are comparable to previous studies. There is no significant difference between the isolated maser and UCHII populations.

(iv) HCO^+ and H^{13}CO^+ are detected towards 99% and 98% of the sample, respectively. Low excitation temperatures derived from HCO^+ lead us to believe that the emission is generally

beam diluted in our 36'' beam, however, self absorption in the HCO^+ line profile may also cause us to underestimate the line brightness. We derived beam averaged column densities assuming a $[\text{HCO}^+]/[\text{H}^{13}\text{CO}^+]$ ratio of 50 and an excitation temperature of 15 K.

(v) Most HCO^+ line profiles exhibit asymmetries due to self-absorption, which may be interpreted as inward or outward motions. Approximately equal numbers of red and blue profiles are found towards UCHII regions, isolated masers and maserless sources.

(vi) The majority of sources with multi-colour MSX fluxes pass the MYSO colour selection criteria of Lumsden et al. (2002). Five maser sources fail the colour cuts and are likely very young massive star-forming cores. Sources with very red MSX colours are indistinguishable from the bulk of the sample in terms of CH_3CN detections and brightness. MSX-dark clouds are notable as CH_3CN is generally brighter than in sources detected in emission with MSX; however this may be as a result of their near distances. Where asymmetric HCO^+ profiles are seen towards MSX-dark clouds they tend to be blue-skewed, indicative of inward motions.

In continuation of this work we will report on the detection of other molecules in a forthcoming paper. We have surveyed the same sources for CH_3OH (2–1), ^{13}CO (1–0), N_2H^+ (1–0), HCN (1–0) and HNC (1–0), also using the Mopra antenna at 3-mm.

ACKNOWLEDGEMENTS

The authors wish to thank the staff of the ATNF for their tireless support of the Mopra telescope since 1999. The Mopra telescope is operated through a collaborative arrangement between the University of New South Wales and the CSIRO. We also wish to thank the Australian research council and UNSW for grant support. CRP was supported by a School of Physics Scholarship during the course of his PhD. EFL gratefully acknowledges support from the ATNF Distinguished Visitor Program, and US National Science Foundation grant AST03-0750. We are also grateful to the anonymous referee

for comments and discussions that helped improve the science and presentation.

REFERENCES

Acord J. M., Churchwell E., Wood D. O. S., 1998, *ApJ*, 495, L107+

Araya E., Hofner P., Kurtz S., Bronfman L., DeDeo S., 2005, *ApJS*, 157, 279

Beltrán M. T., Cesaroni R., Neri R., Codella C., Furuya R. S., Testi L., Olmi L., 2005, *A&A*, 435, 901

Brand J., Blitz L., 1993, *A&A*, 275, 67

Cesaroni R., Hofner P., Walmsley C. M., Churchwell E., 1998, *A&A*, 331, 709

Churchwell E., Walmsley C. M., Cesaroni R., 1990, *A&AS*, 83, 119

Churchwell E., Walmsley C. M., Wood D. O. S., 1992, *A&A*, 253, 541

Codella C., Welser R., Henkel C., Benson P. J., Myers P. C., 1997, *A&A*, 324, 203

De Vries C. H., Myers P. C., 2005, *ApJ*, 620, 800

Downes D., Wilson T. L., Bieging J., Wink J., 1980, *A&AS*, 40, 379

Dunne L., Eales S., Edmunds M., Ivison R., Alexander P., Clements D. L., 2000, *MNRAS*, 315, 115

Egan M. P., Price S. D., 1996, *AJ*, 112, 2862

Emerson J. P., 1988, in *NATO ASIC Proc. 241: Formation and Evolution of Low Mass Stars Infrared Emission Processes*. pp 21–44

Faúndez S., Bronfman L., Garay G., Chini R., Nyman L.-Å., May J., 2004, *A&A*, 426, 97

Girart J. M., Estalella R., Ho P. T. P., Rudolph A. L., 2000, *ApJ*, 539, 763

Goldsmith P. F., Langer W. D., 1999, *ApJ*, 517, 209

Hanson M. M., Howarth I. D., Conti P. S., 1997, *ApJ*, 489, 698

Hatchell J., Thompson M. A., Millar T. J., MacDonald G. H., 1998, *A&AS*, 133, 29

Hill T., Burton M. G., Thompson M. A., Walsh A. J., Hunt-Cunningham M., Garay G., 2005, *MNRAS*

Hofner P., Kurtz S., Churchwell E., Walmsley C. M., Cesaroni R., 1994, *ApJ*, 429, L85

Hollis J. M., 1982, *ApJ*, 260, 159

James A., Dunne L., Eales S., Edmunds M. G., 2002, *MNRAS*, 335, 753

Kramer C., Richer J., Mookerjea B., Alves J., Lada C., 2003, *A&A*, 399, 1073

Kurtz S., Cesaroni R., Churchwell E., Hofner P., Walmsley C. M., 2000, *Protostars and Planets IV*, pp 299–+

Kurtz S., Churchwell E., Wood D. O. S., 1994, *ApJS*, 91, 659

Kutner M. L., Ulich B. L., 1981, *ApJ*, 250, 341

Ladd E. F., Purcell C. R., Wong T., Robertson S., 2005, *PASA*, 22, 62

Larionov G. M., Val'tts I. E., Winnberg A., Johansson L. E. B., Booth R. S., Golubev V. V., 1999, *A&AS*, 139, 257

Loren R. B., Mundy L. G., 1984, *ApJ*, 286, 232

Lumsden S. L., Hoare M. G., Oudmaijer R. D., Richards D., 2002, *MNRAS*, 336, 621

Mackay D. D. S., 1999, *MNRAS*, 304, 61

Mardones D., Myers P. C., Tafalla M., Wilner D. J., Bachiller R., Garay G., 1997, *ApJ*, 489, 719

Menten K. M., 1991, *ApJ*, 380, L75

Mezger P. G., Henderson A. P., 1967, *ApJ*, 147, 471

Millar T. J., MacDonald G. H., Gibb A. G., 1997, *A&A*, 325, 1163

Minh Y. C., Irvine W. M., Ohishi M., Ishikawa S., Saito S., Kaifu N., 1993, *A&A*, 267, 229

Minier V., Burton M. G., Hill T., Pestalozzi M. R., Purcell C. R., Garay G., Walsh A. J., Longmore S., 2005, *A&A*, 429, 945

Minier V., Conway J. E., Booth R. S., 2001, *A&A*, 369, 278

Molinari S., Brand J., Cesaroni R., Palla F., 1996, *A&A*, 308, 573

Nummelin A., Bergman P., Hjalmarsen Å., Friberg P., Irvine W. M., Millar T. J., Ohishi M., Saito S., 2000, *ApJS*, 128, 213

Olmi L., Cesaroni R., Hofner P., Kurtz S., Churchwell E., Walmsley C. M., 2003, *A&A*, 407, 225

Olmi L., Cesaroni R., Walmsley C. M., 1993, *A&A*, 276, 489

Panagia N., 1973, *AJ*, 78, 929

Pankonin V., Churchwell E., Watson C., Bieging J. H., 2001, *ApJ*, 558, 194

Pickett, H. M., Poynter R. L., Cohen E. A., Delitsky M. L., Pearson J. C., Muller, H. S. P., 1998, *JQS&RT*, 60, 883

Pratap P., Megeath S. T., Bergin E. A., 1999, *ApJ*, 517, 799

Rawlings J. M. C., Redman M. P., Keto E., Williams D. A., 2004, *MNRAS*, 351, 1054

Rawlings J. M. C., Taylor S. D., Williams D. A., 2000, *MNRAS*, 313, 461

Remijan A., Sutton E. C., Snyder L. E., Friedel D. N., Liu S.-Y., Pei C.-C., 2004, *ApJ*, 606, 917

Savage C., Apponi A. J., Ziurys L. M., Wyckoff S., 2002, *ApJ*, 578, 211

Solomon P. M., Rivolo A. R., Barrett J., Yahil A., 1987, *ApJ*, 319, 730

Stier M. T., Jaffe D. T., Rengarajan T. N., Fazio G. G., Maxson C. W., McBreen B., Loughran L., Serio S., Sciortino S., 1984, *ApJ*, 283, 573

Turner B. E., 1991, *ApJS*, 76, 617

van Dishoeck E. F., Blake G. A., 1998, *ARA&A*, 36, 317

Walsh A. J., Burton M. G., Hyland A. R., Robinson G., 1998, *MNRAS*, 301, 640

Walsh A. J., Burton M. G., Hyland A. R., Robinson G., 1999, *MNRAS*, 309, 905

Walsh A. J., Hyland A. R., Robinson G., Burton M. G., 1997, *MNRAS*, 291, 261

Walsh A. J., Macdonald G. H., Alvey N. D. S., Burton M. G., Lee J.-K., 2003, *A&A*, 410, 597

Wilner D. J., Wright M. C. H., Plambeck R. L., 1994, *ApJ*, 422, 642

Wink J. E., Altenhoff W. J., Mezger P. G., 1982, *A&A*, 108, 227

Wood D. O. S., Churchwell E., 1989, *ApJ*, 340, 265

Wu J., Evans N. J., 2003, *ApJ*, 592, L79

Table 1. Details of observed transitions

Species	Transition ^α	Frequency (GHz)	E _u /k (K)	A _{ul} ^β (×10 ⁻⁵ s ⁻¹)	g _{JK} ^γ
CH ₃ CN	5 ₀ → 4 ₀	91.987054	13.24	6.121	44
	5 ₁ → 4 ₁	91.985284	20.39	5.875	44
	5 ₂ → 4 ₂	91.980000	41.82	5.139	44
	5 ₃ → 4 ₃	91.971374	77.53	3.913	88
	5 ₄ → 4 ₄	91.959206	127.51	2.200	44
	6 ₀ → 5 ₀	110.383494	18.54	10.895	52
	6 ₁ → 5 ₁	110.381376	25.68	10.592	52
	6 ₂ → 5 ₂	110.374968	47.11	9.681	52
	6 ₃ → 5 ₃	110.364470	82.82	8.166	104
	6 ₄ → 5 ₄	110.349760	134.25	6.045	52
HCO ⁺	1 → 0	89.188526	4.28	3.02	3
H ¹³ CO ⁺	1 → 0	86.754330	4.16	2.80	3

^α J_K quantum numbers.

^β Einstein A coefficients for symmetric tops and linear rotors are given by $(16\pi^3\nu^3\mu^2S)/(3\epsilon_0hc^3g_u)$ where $g_u = (2J + 1)$ and μ is the electric dipole moment for the molecule. Other constants take their usual values and are in SI units.

^γ $g_{JK} = g_u S(I, J)$ is the degeneracy of the J_K rotational level as given by Araya et al. (2005), matched with the partition function quoted in the same paper. $S(I, J) = (J^2 - K^2)/J$ is the intrinsic line strength.

Table 2. Details of the 83 sources observed.

Galactic Name	Right Ascension (J2000)	Declination (J2000)	Velocity (LSR) (km s ⁻¹)	Adopted ^α Distance (kpc)	Luminosity ^β (×10 ⁴ L _⊙)	Single Star Type ^γ	Other ^δ Associations		Molecular Cloud Name
G0.21+0.00	17:46:07.7	-28:45:20	44.6	8.4 ^t	11.9	O8	M	R	MIR
G0.26+0.01	17:46:11.3	-28:42:48	26.0	8.4 ^t	—	—	M	—	DRK
G0.32-0.20	17:47:09.1	-28:46:16	18.9	8.5 ^t	39.9	O6	M	R	MIR
G0.50+0.19	17:46:04.0	-28:24:51	-6.1	2.6 ^p	0.9	B1	M	—	MIR
G0.55-0.85	17:50:14.5	-28:54:31	17.5	8.5 ^t	85.5	O5	M	R	MIR
G0.84+0.18	17:46:52.8	-28:07:35	5.9	5.6	3.7	O9.5	M	—	MIR
G1.15-0.12	17:48:48.5	-28:01:12	-17.2	8.5	10.9	O8	M	—	MIR
G2.54+0.20	17:50:46.5	-26:39:45	10.1	4.4 ^r	—	—	M	—	DRK
G5.89-0.39	18:00:31.0	-24:03:59	9.3	2.0 ^a	14.7	O7.5	M	R	MIR
G5.90-0.43	18:00:40.9	-24:04:21	7.0	2.0 ^d	6.8	O9.5	M	—	MIR
G5.90-0.44	18:00:43.9	-24:04:47	9.5	2.5 ^d	3.7	B0	M	—	MIR
G6.54-0.11	18:00:50.9	-23:21:29	0.0	14.9 ^w	37.2	O6	M	—	MIR
G6.61-0.08	18:00:54.0	-23:17:02	7.7	14.9	5.7	O9.5	M	—	MIR
G8.14+0.23	18:03:00.8	-21:48:10	19.2	3.3 ^w	8.5	O8.5	M	R	MIR
G8.67-0.36	18:06:19.0	-21:37:32	34.8	4.5 ^d	7.4	O9	M	R	MIR
G8.68-0.37	18:06:23.5	-21:37:11	37.2	4.8 ^d	—	—	M	—	DRK
G9.62+0.19	18:06:14.8	-20:31:37	4.4	5.7 ^{ho}	28.0	O6.5	M	R	MIR
G9.99-0.03	18:07:50.1	-20:18:57	48.9	5.0	2.0	BO.5	M	—	MIR
G10.10-0.72	18:05:18.2	-19:51:14	-4.0	16	—	—	M	—	—
G10.29-0.13	18:08:49.4	-20:05:59	13.7	2.2 ^d	1.1	B1	M	—	MIR
G10.30-0.15	18:08:55.5	-20:05:58	13.0	2.1 ^d	6.6	O9.5	M	R	MIR
G10.32-0.16	18:09:01.5	-20:05:08	12.2	2.2 ^d	8.1	O9	M	—	MIR
G10.34-0.14	18:09:00.0	-20:03:36	12.2	2.2 ^d	1.7	B0.5	M	—	MIR
G10.44-0.02	18:08:44.9	-19:54:38	75.4	6.0 ^r	—	—	M	—	DRK
G10.47+0.03	18:08:38.2	-19:51:50	67.0	5.7 ^{ce}	23.0	O6.5	M	R	MIR
G10.48+0.03	18:08:37.9	-19:51:15	66.2	5.7 ^{ce}	—	—	M	—	DRK
G10.63-0.33	18:10:18.0	-19:54:05	-4.1	6.0 ^d	56.8	O5.5	M	—	MIR
G10.63-0.38	18:10:29.2	-19:55:41	-3.1	6.0 ^d	26.4	O6.5	M	R	MIR
G11.50-1.49	18:16:22.1	-19:41:28	10.3	1.6	0.5	B2	M	—	MIR
G11.94-0.15	18:12:17.3	-18:40:03	42.6	4.4	0.6	B2	M	—	MIR
G11.94-0.62	18:14:00.9	-18:53:27	37.9	4.1 ^{ch}	7.6	O9	M	R	MIR
G11.99-0.27	18:12:51.2	-18:40:40	59.7	5.2	1.2	B1	M	—	MIR
G12.03-0.03	18:12:01.9	-18:31:56	110.5	6.7	1.3	B0.5	M	—	MIR
G12.18-0.12	18:12:41.0	-18:26:22	26.5	13.4 ^d	—	—	M	—	MIR
G12.21-0.09	18:12:37.5	-18:24:08	23.8	13.6 ^d	—	—	M	—	MIR
G12.68-0.18	18:13:54.7	-18:01:41	56.5	4.9 ^s	1.5	B0.5	M	—	MIR
G12.72-0.22	18:14:07.0	-18:00:37	34.2	3.7 ^s	4.7	B0	M	—	MIR
G12.89+0.49	18:11:51.4	-17:31:30	33.3	3.6 ^m	3.4	B0	M	—	MIR
G12.91-0.26	18:14:39.5	-17:52:00	37.0	3.9 ^s	7.3	O9.5	M	—	MIR
G14.60+0.02	18:17:01.1	-16:14:39	24.7	2.8 ^d	1.0	B1	M	R	MIR
G14.99-0.70	18:20:23.1	-16:14:43	18.7	1.6 ^h	—	—	M	—	DRK
G15.03-0.68	18:20:24.8	-16:11:35	19.5	1.6 ^h	16.3	O7	M	—	MIR
G15.03-0.71	18:20:30.3	-16:12:43	21.0	1.6 ^h	3.1	B0	M	—	MIR
G16.59-0.05	18:21:09.1	-14:31:49	59.9	4.6 ^{co}	2.5	B0.5	M	—	MIR
G16.86-2.16	18:29:24.4	-15:16:04	17.8	1.9	0.4	B2	M	—	MIR
G19.36-0.03	18:26:25.2	-12:03:53	26.7	2.5	0.5	B2	M	—	MIR
G19.47+0.17	18:25:54.7	-11:52:34	19.7	1.9	1.3	B0.5	M	—	MIR
G19.49+0.15	18:26:00.4	-11:52:22	23.0	2.2	0.6	B2	M	—	MIR
G19.61-0.13	18:27:16.4	-11:53:38	56.9	4.2 ^d	2.1	B0.5	M	—	MIR
G19.70-0.27	18:27:55.9	-11:52:39	43.0	3.5	0.6	B2	M	—	MIR
G21.88+0.01	18:31:01.7	-09:49:01	23.3	2.0	—	—	M	—	—
G22.36+0.07	18:31:44.1	-09:22:13	84.1	10.5 ^s	7.9	O9	M	—	MIR
G23.26-0.24	18:34:31.8	-08:42:47	61.5	4.2	2.6	B0.5	M	—	MIR
G23.44-0.18	18:34:39.2	-08:31:32	101.6	5.9 ^d	—	—	M	—	DRK
G23.71-0.20	18:35:12.4	-08:17:40	69.0	4.5	1.6	B0.5	M	—	MIR
G24.79+0.08	18:36:12.3	-07:12:11	110.5	7.7 ^{be}	20.4	O6.5	M	—	MIR
G24.85+0.09	18:36:18.4	-07:08:52	108.9	6.3 ^{co}	10.8	O8	M	—	MIR
G25.65+1.05	18:34:20.9	-05:59:40	42.4	3.1 ^m	2.5	B0.5	M	R	MIR

Table 2 – *continued*

Galactic Name	Right Ascension (J2000)	Declination (J2000)	Velocity (LSR) (km s ⁻¹)	Adopted ^α Distance (kpc)	Luminosity ^β (×10 ⁴ L _⊙)	Single ^γ Star Type	Other ^δ Associations		Molecular Cloud Name
G25.71+0.04	18:38:03.1	-06:24:15	98.7	9.5 ^d	8.9	O8.5	M	-	MIR
G25.83-0.18	18:39:03.6	-06:24:10	93.4	5.6 ^r	-	-	M	-	DRK
G28.15+0.00	18:42:42.2	-04:15:32	98.6	5.9	2.0	B0.5	M	-	MIR
G28.20-0.05	18:42:58.1	-04:13:56	95.6	6.8 ^r	17.1	O7 M	R	MIR	
G28.28-0.36	18:44:13.3	-04:18:03	48.9	3.3 ^{so}	-	-	M	R	-
G28.31-0.39	18:44:22.0	-04:17:38	86.2	5.2 ^{so}	4.0	B0	M	-	MIR
G28.83-0.25	18:44:51.1	-03:45:48	87.1	5.3 ^{so}	3.5	B0	M	-	MIR
G29.87-0.04	18:46:00.0	-02:44:58	100.9	6.3	5.3	B0	M	-	MIR
G29.96-0.02	18:46:04.8	-02:39:20	97.6	6.0 ^p	74.0	O5	M	R	MIR
G29.98-0.04	18:46:12.1	-02:38:58	101.6	6.3 ^r	-	-	M	-	DRK
G30.59-0.04	18:47:18.6	-02:06:07	41.8	11.8 ^{so}	32.6	O6	M	-	MIR
G30.71-0.06	18:47:36.5	-02:00:31	92.8	5.8 ^r	-	-	M	R	DRK
G30.76-0.05	18:47:39.7	-01:57:22	93.0	5.8 ^r	12.1	O8	M	-	MIR
G30.78+0.23	18:46:41.5	-01:48:32	41.8	2.9	-	-	M	-	MIR
G30.79+0.20	18:46:48.1	-01:48:46	81.6	5.1 ^r	2.3	B0.5	M	-	DRK
G30.82-0.05	18:47:46.5	-01:54:17	96.6	6.0 ^r	2.7	B0.5	M	-	DRK
G30.82+0.28	18:46:36.1	-01:45:18	97.8	8.5 ^l	-	-	M	-	MIR
G30.90+0.16	18:47:09.2	-01:44:09	106.2	7.3 ^t	4.8	B0	M	-	MIR
G31.28+0.06	18:48:12.4	-01:26:23	109.4	7.2 ^t	12.0	O8	M	R	MIR
G31.41+0.31	18:47:34.3	-01:12:47	96.7	7.9 ^{ce}	17.0	O7	M	R	MIR
G316.81-0.06	14:45:26.9	-59:49:16	-38.7	2.7	13.2	O7.5	M	-	MIR
G318.95-0.20	15:00:55.3	-58:58:54	-34.5	2.4	2.9	B0.5	M	-	MIR
G323.74-0.26	15:31:45.8	-56:30:50	-49.6	3.3	5.3	B0	M	-	MIR
G331.28-0.19	16:11:26.9	-51:41:57	-88.1	5.4	23.0	O6.5	M	-	MIR
G332.73-0.62	16:20:02.7	-51:00:32	-50.2	3.5	-	-	M	-	DRK

^α The distance given in column 5 is the assumed kinematic distance, in kpc, based on the rotation curve of Brand & Blitz (1993). We have resolved the kinematic distance ambiguity for 58 sources, mainly using the work of the following authors: ^a Acord et al. (1998), ^{ho} Hofner et al. (1994), ^{be} Beltrán et al. (2005), ^p Pratap et al. (1999), ^d Downes et al. (1980), ^w Wink et al. (1982), ^{ch} Churchwell et al. (1990), ^{ce} Cesaroni et al. (1998), ^m Molinari et al. (1996), ^{so} Solomon et al. (1987), ^{co} Codella et al. (1997), ^l Larionov et al. (1999), ^h Hanson et al. (1997), ^s Stier et al. (1984). Also, the near and far distances for sources marked with a ‘t’ were within 1 kpc and they were placed at the middle distance. Sources marked with a ‘r’ were seen in absorption at 8μm (dark clouds) and were placed at the near distance. The remaining 25 sources were assumed to lie at the near distance except for G10.10-0.72.

^β Bolometric luminosities were calculated from a two component greybody fit to the SED containing SCUBA and MSX fluxes (Walsh et al. 2003). The IRAS fluxes were included in the fit only if known with confidence. Sources without a quoted luminosity had insufficient data to constrain a fit.

^γ Approximate spectral types for a given luminosity were read from Table 1 of Panagia (1973).

^δ ‘M’ indicates a 6.7 GHz methanol-maser at the position. ‘R’ indicates a UCH_{II} region lies within the Mopra beam. ‘MIR’ indicates a detection of mid-infrared MSX emission near the source, ‘DRK’ indicates the source is associated with a MSX dark cloud.

Table 3. Summary of detections towards observed sources.

Source	CH_3CN $^\alpha$	HCO^+	$H^{13}CO^+$	$21\mu m$ $^\beta$	$8\mu m$ $^\beta$	Source	CH_3CN $^\alpha$	HCO^+	$H^{13}CO^+$	$21\mu m$ $^\beta$	$8\mu m$ $^\beta$
G0.21+0.00	n -	y	n	y	y	G15.03-0.71	n -	y	y	y	y
G0.26+0.01	y -	y	y	d	d	G16.59-0.05	y -	y	y	y	y
G0.32-0.20	y -	y	y	y	y	G16.86-2.16	y y	y	y	y	y
G0.50+0.19	n -	y	y	y	y	G19.36-0.03	y -	y	y	y	y
G0.55-0.85	y y	y	y	y	y	G19.47+0.17	y n	y	y	y	y
G0.84+0.18	y n	y	y	y	y	G19.49+0.15	n -	y	y	y	y
G1.15-0.12	y n	y	y	y	y	G19.61-0.13	y -	y	y	y	y
G2.54+0.20	n -	y	y	n	d	G19.70-0.27	n -	y	y	y	y
G5.89-0.39	y -	y	y	y	y	G21.88+0.01	n -	y	y	n	n
G5.90-0.43	y y	y	y	y	y	G22.36+0.07	y -	y	y	y	y
G5.90-0.44	y -	y	y	y	y	G23.26-0.24	n -	y	y	n	y
G6.54-0.11	n -	y	n	y	y	G23.44-0.18	y y	y	y	n	d
G6.61-0.08	n -	y	y	y	y	G23.71-0.20	n -	y	y	y	y
G8.14+0.23	y -	y	y	y	y	G24.79+0.08	y y	y	y	y	n
G8.67-0.36	y -	y	y	y	y	G24.85+0.09	n -	y	y	y	y
G8.68-0.37	y -	y	y	n	d	G25.65+1.05	y -	y	y	y	y
G9.62+0.19	y n	y	y	y	y	G25.71+0.04	y -	y	y	y	n
G9.99-0.03	y -	y	y	y	y	G25.83-0.18	y y	y	y	n	d
G10.10+0.72	n -	n	n	n	n	G28.15+0.00	y -	y	y	y	y
G10.29-0.13	y n	y	y	y	y	G28.20-0.05	y -	y	y	y	y
G10.30-0.15	y y	y	y	y	y	G28.28-0.36	y -	y	y	n	n
G10.32-0.16	y y	y	y	y	y	G28.31-0.39	n -	y	y	y	y
G10.34-0.14	y y	y	y	n	y	G28.83-0.25	y -	y	y	y	n
G10.44-0.02	y y	y	y	n	d	G29.87-0.04	n -	y	y	y	y
G10.47+0.03	y -	y	y	y	y	G29.96-0.02	y y	y	y	y	y
G10.48+0.03	y -	y	y	n	d	G29.98-0.04	y y	y	y	n	d
G10.63-0.33	n -	y	y	y	y	G30.59-0.04	n -	y	y	y	y
G10.63-0.38	y y	y	y	y	y	G30.71-0.06	y y	y	y	d	d
G11.50-1.49	n -	y	y	y	y	G30.76-0.05	y y	y	y	y	y
G11.94-0.15	n -	y	y	y	y	G30.78+0.23	n -	y	y	n	y
G11.94-0.62	y y	y	y	y	y	G30.79+0.20	y -	y	y	y	d
G11.99-0.27	n -	y	y	y	y	G30.82-0.05	y y	y	y	n	d
G12.03-0.03	n -	y	y	y	y	G30.82+0.28	n -	y	y	y	y
G12.18-0.12	n -	y	y	y	n	G30.90+0.16	y -	y	y	y	y
G12.21-0.09	n -	y	y	y	n	G31.28+0.06	y y	y	y	y	y
G12.68-0.18	y y	y	y	y	y	G31.41+0.31	y y	y	y	y	y
G12.72-0.22	y -	y	y	y	y	G316.81-0.06	y y	y	y	y	y
G12.89+0.49	y n	y	y	y	y	G318.95-0.20	y n	y	y	y	y
G12.91-0.26	y y	y	y	y	y	G323.74-0.26	y y	y	y	y	n
G14.60+0.02	y -	y	y	y	n	G331.28-0.19	y n	y	y	y	y
G14.99-0.70	y -	y	y	n	d	G332.73-0.62	y n	y	y	d	d
G15.03-0.68	y y	y	y	y	y	% Detections $^\gamma$:	70	99	98	78	72

$^\alpha$ 33 sources were searched for both CH_3CN (5–4) (first entry), and CH_3CN (6–5) (second entry).

$^\beta$ MSX dark clouds seen in absorption against background radiation at 8 or 21 μm are marked with a ‘d’.

$^\gamma$ If dark clouds are counted then the detection rate rises to 82 % and 88 % for the 21 and 8 μm MSX bands respectively.

Table 4. CH₃CN Line Parameters.

Source ^α	V _{LSR} ^β (km s ⁻¹)	δV (km s ⁻¹)	T _{MB} dv, K=0 (K km s ⁻¹)	T _{MB} dv, K=1 (K km s ⁻¹)	T _{MB} dv, K=2 (K km s ⁻¹)	T _{MB} dv, K=3 (K km s ⁻¹)	T _{MB} dv, K=4 (K km s ⁻¹)
G0.32-0.20	18.09	2.87	0.29 ± 0.13	0.25 ± 0.12	–	–	–
G0.55-0.85	17.22	5.66	5.47 ± 0.12	4.52 ± 0.11	2.73 ± 0.11	2.41 ± 0.12	0.90 ± 0.11
	18.32	7.87	2.56 ± 0.24	1.98 ± 0.23	1.87 ± 0.15	1.27 ± 0.15	–
G0.84+0.18	5.89	2.72	0.37 ± 0.06	0.24 ± 0.06	–	–	–
G1.15-0.12	-16.80	2.92	0.54 ± 0.12	0.46 ± 0.13	–	–	–
G5.89-0.39	9.20	4.54	2.73 ± 0.09	2.49 ± 0.09	1.48 ± 0.09	1.10 ± 0.09	–
G5.90-0.43	7.39	4.87	3.39 ± 0.30	2.80 ± 0.29	1.68 ± 0.30	1.01 ± 0.28	–
	7.23	5.12	2.75 ± 0.21	1.84 ± 0.21	1.25 ± 0.20	0.96 ± 0.19	–
G5.90-0.44	9.73	2.63	1.02 ± 0.08	0.66 ± 0.07	0.31 ± 0.07	0.22 ± 0.07	–
G8.14+0.23	18.60	4.34	0.91 ± 0.10	0.66 ± 0.10	0.32 ± 0.10	0.29 ± 0.10	–
G8.67-0.36	35.02	5.06	2.74 ± 0.10	2.48 ± 0.10	1.31 ± 0.10	0.76 ± 0.09	0.24 ± 0.09
G8.68-0.37	38.01	4.40	2.29 ± 0.09	2.25 ± 0.09	0.96 ± 0.09	0.72 ± 0.09	0.26 ± 0.09
G9.62+0.19	4.56	6.72	3.41 ± 0.27	2.13 ± 0.25	1.59 ± 0.19	1.39 ± 0.20	–
G9.99-0.03	49.56	4.48	0.34 ± 0.08	0.29 ± 0.08	0.13 ± 0.07	–	–
G10.29-0.13	13.40	4.81	2.01 ± 0.17	1.46 ± 0.17	0.68 ± 0.16	–	–
G10.30-0.15	12.88	5.39	2.80 ± 0.37	2.39 ± 0.36	0.85 ± 0.33	0.54 ± 0.32	–
	12.37	4.03	0.89 ± 0.14	0.77 ± 0.14	–	–	–
G10.32-0.16	12.17	5.10	1.36 ± 0.21	1.13 ± 0.20	0.66 ± 0.22	0.56 ± 0.22	–
	11.69	3.56	0.51 ± 0.06	0.39 ± 0.05	0.27 ± 0.05	–	–
G10.34-0.14	12.07	4.55	1.24 ± 0.23	0.81 ± 0.22	0.37 ± 0.20	0.23 ± 0.20	–
	12.51	3.92	1.44 ± 0.13	1.31 ± 0.12	0.41 ± 0.12	–	–
G10.44-0.02	73.28	4.20	0.38 ± 0.09	0.15 ± 0.09	–	–	–
	75.56	5.49	0.72 ± 0.15	0.75 ± 0.20	–	–	–
G10.47+0.03	67.31	11.32	7.70 ± 0.48	5.02 ± 0.45	6.89 ± 0.28	6.53 ± 0.26	3.93 ± 0.25
G10.48+0.03	66.34	9.03	2.40 ± 0.33	1.59 ± 0.31	1.38 ± 0.18	1.00 ± 0.18	–
G10.63-0.38	-3.69	6.69	4.26 ± 0.25	3.59 ± 0.25	2.01 ± 0.18	1.62 ± 0.18	–
	-4.81	6.85	2.76 ± 0.27	3.17 ± 0.28	1.29 ± 0.17	1.50 ± 0.18	–
G11.94-0.62	38.11	4.24	1.74 ± 0.17	1.46 ± 0.16	0.58 ± 0.15	–	–
	38.11	3.83	0.64 ± 0.13	0.41 ± 0.12	0.27 ± 0.13	–	–
G12.68-0.18	55.99	4.13	0.86 ± 0.10	0.77 ± 0.10	0.37 ± 0.09	–	–
	56.73	4.89	0.92 ± 0.18	0.81 ± 0.19	0.85 ± 0.21	0.59 ± 0.19	–
G12.72-0.22	34.40	5.80	0.66 ± 0.13	0.44 ± 0.13	0.21 ± 0.12	–	–
G12.89+0.49	33.28	4.31	1.24 ± 0.16	1.32 ± 0.16	0.78 ± 0.17	1.05 ± 0.17	–
G12.91-0.26	37.40	4.18	1.07 ± 0.23	0.79 ± 0.21	0.33 ± 0.20	–	–
	37.47	5.03	2.22 ± 0.16	2.65 ± 0.16	1.56 ± 0.16	1.87 ± 0.17	–
G14.60+0.02	26.40	5.43	0.48 ± 0.05	0.67 ± 0.06	0.29 ± 0.05	0.26 ± 0.05	–
G14.99-0.70	19.09	6.51	1.61 ± 0.29	0.90 ± 0.27	0.94 ± 0.24	–	–
G15.03-0.68	19.99	4.38	0.67 ± 0.10	0.51 ± 0.10	0.11 ± 0.10	–	–
	19.65	3.42	0.86 ± 0.09	0.84 ± 0.09	0.60 ± 0.09	–	–
G16.59-0.05	59.91	5.00	1.21 ± 0.32	1.50 ± 0.33	0.53 ± 0.31	–	–
G16.86-2.16	18.14	5.79	1.41 ± 0.34	1.28 ± 0.33	0.49 ± 0.28	0.34 ± 0.30	–
	17.98	4.59	1.18 ± 0.17	1.66 ± 0.18	0.67 ± 0.17	0.40 ± 0.17	–
G19.36-0.03	25.83	3.87	0.55 ± 0.11	0.53 ± 0.10	–	–	–
G19.47+0.17	20.31	6.04	1.93 ± 0.25	2.01 ± 0.26	0.99 ± 0.24	0.81 ± 0.23	–
G19.61-0.13	57.07	5.68	0.43 ± 0.16	0.69 ± 0.17	–	–	–
G22.36+0.07	84.31	1.62	0.17 ± 0.04	0.11 ± 0.04	–	–	–
G23.44-0.18	101.64	5.43	2.18 ± 0.17	1.88 ± 0.16	0.80 ± 0.15	0.83 ± 0.15	–
	102.48	5.45	2.45 ± 0.18	2.00 ± 0.18	0.89 ± 0.16	1.06 ± 0.17	–
G24.79+0.08	110.81	6.63	3.60 ± 0.22	3.42 ± 0.21	2.38 ± 0.20	1.92 ± 0.20	0.45 ± 0.18
	112.03	5.94	3.68 ± 0.22	3.58 ± 0.22	2.45 ± 0.21	2.55 ± 0.21	–
G25.65+1.05	42.55	4.55	1.11 ± 0.21	0.93 ± 0.21	0.78 ± 0.23	–	–
G25.71+0.04	99.01	5.26	0.45 ± 0.11	0.16 ± 0.11	0.19 ± 0.09	–	–
G25.83-0.18	93.81	5.25	2.13 ± 0.15	1.89 ± 0.15	0.92 ± 0.15	0.87 ± 0.14	0.33 ± 0.14
	94.38	5.27	1.84 ± 0.17	1.88 ± 0.17	0.96 ± 0.17	–	–
G28.15+0.00	98.95	3.22	0.54 ± 0.12	0.49 ± 0.12	0.20 ± 0.11	–	–
G28.20-0.05	95.86	5.83	1.19 ± 0.25	1.46 ± 0.26	1.31 ± 0.25	0.59 ± 0.22	–
G28.28-0.36	48.69	4.09	0.58 ± 0.11	0.41 ± 0.11	–	–	–
G28.83-0.25	86.83	2.70	0.67 ± 0.15	0.46 ± 0.14	0.32 ± 0.14	–	–

Table 4 – *continued*

Source $^{\alpha}$	V_{LSR}^{β} (km s^{-1})	δV (km s^{-1})	T_{MB} dv, K=0 (K km s^{-1})	T_{MB} dv, K=1 (K km s^{-1})	T_{MB} dv, K=2 (K km s^{-1})	T_{MB} dv, K=3 (K km s^{-1})	T_{MB} dv, K=4 (K km s^{-1})
G29.96–0.02	97.75	5.02	2.02 ± 0.26	1.52 ± 0.24	1.24 ± 0.26	1.02 ± 0.26	0.24 ± 0.23
	97.12	6.53	2.21 ± 0.25	1.13 ± 0.22	1.50 ± 0.20	1.50 ± 0.23	–
G29.98–0.04	102.27	8.76	0.79 ± 0.10	0.46 ± 0.17	–	–	–
	100.49	3.02	0.71 ± 0.20	0.64 ± 0.20	–	–	–
G30.71–0.06	91.19	4.60	3.36 ± 0.29	3.03 ± 0.29	1.41 ± 0.28	1.35 ± 0.28	0.60 ± 0.27
	91.37	4.89	2.22 ± 0.22	1.98 ± 0.21	1.28 ± 0.23	1.43 ± 0.23	–
G30.76–0.05	92.65	4.18	0.67 ± 0.12	0.69 ± 0.12	0.15 ± 0.12	–	–
	98.26	2.15	1.35 ± 0.33	0.68 ± 0.22	–	–	–
G30.79+0.20	81.39	4.28	0.61 ± 0.26	0.76 ± 0.26	0.29 ± 0.25	–	–
G30.82–0.05	98.59	6.48	5.98 ± 0.44	4.82 ± 0.38	2.92 ± 0.33	2.18 ± 0.32	0.73 ± 0.31
	98.10	7.24	5.48 ± 0.33	3.88 ± 0.29	2.81 ± 0.23	3.36 ± 0.23	–
G30.90+0.16	105.62	4.19	0.43 ± 0.13	0.25 ± 0.12	–	–	–
G31.28+0.06	109.47	4.11	1.12 ± 0.29	1.13 ± 0.29	0.45 ± 0.28	–	–
	108.68	1.61	0.60 ± 0.12	0.32 ± 0.11	–	–	–
G31.41+0.31	97.64	7.44	2.64 ± 0.31	2.26 ± 0.29	2.56 ± 0.26	2.33 ± 0.29	1.04 ± 0.25
	98.11	7.33	3.83 ± 0.24	3.35 ± 0.23	3.02 ± 0.20	2.88 ± 0.21	–
G316.81–0.06	–39.69	3.70	0.99 ± 0.14	0.83 ± 0.14	0.67 ± 0.14	0.49 ± 0.14	–
	–43.70	7.44	0.24 ± 0.33	1.22 ± 0.36	–	–	–
G318.95–0.20	–34.68	4.47	1.48 ± 0.12	1.25 ± 0.12	0.76 ± 0.12	0.58 ± 0.12	–
G323.74–0.26	–50.11	4.30	1.55 ± 0.12	1.22 ± 0.11	0.82 ± 0.12	0.75 ± 0.12	–
	–48.73	2.90	0.85 ± 0.15	0.64 ± 0.14	–	–	–
G331.28–0.19	–87.85	5.36	1.60 ± 0.17	1.24 ± 0.16	0.94 ± 0.14	0.81 ± 0.14	–
G332.73–0.62	–50.74	2.55	0.37 ± 0.10	0.30 ± 0.09	–	–	–

$^{\alpha}$ For each source the parameters of the CH_3CN (5–4) fits are presented in the upper row and those of the CH_3CN (6–5) fits are presented in the lower row.

$^{\beta}$ Quoted V_{LSR} is referenced to the K=0 component.

Table 5. Sources without detected CH₃CN.

Source	rms-noise ^α (mK)
G0.21+0.00	0.101
G0.50+0.19	0.060
G2.54+0.20	0.149
G6.54−0.11	0.075
G6.61−0.08	0.108
G10.10+0.72	0.054
G10.63−0.33	0.087
G11.50−1.49	0.143
G11.94−0.15	0.082
G11.99−0.27	0.080
G12.03−0.03	0.083
G12.18−0.12	0.096
G12.21−0.09	0.099
G15.03−0.71	0.064
G19.49+0.15	0.082
G19.70−0.27	0.074
G21.88+0.01	0.036
G23.26−0.24	0.093
G23.71−0.20	0.088
G24.85+0.09	0.098
G28.31−0.39	0.079
G29.87−0.04	0.106
G30.59−0.04	0.093
G30.78+0.23	0.089
G30.82+0.28	0.064

^α 1 σ noise in the CH₃CN (5−4) spectrum.

Table 6. HCO⁺ and H¹³CO⁺ Line Parameters.

Source	HCO ⁺ Gaussian Fits ^α			HCO ⁺ Integrated Lines ^β			H ¹³ CO ⁺ Gaussian Fits		
	T _{MB} dv (K km s ⁻¹)	V _{LSR} (km s ⁻¹)	δV (km s ⁻¹)	T _{MB} dv (K km s ⁻¹)	Equivalent Width (km s ⁻¹)	Peak T _{MB} (K)	T _{MB} dv (K km s ⁻¹)	V _{LSR} (km s ⁻¹)	δV (km s ⁻¹)
G0.21+0.00	–	–	–	151.18 ± 5.05	55.47	1.85	–	–	–
G0.26+0.01	–	–	–	113.12 ± 5.34	35.39	1.67	–	–	–
G0.32–0.20	35.02 ± 0.28	18.70 ± 0.01	3.66 ± 0.04	29.63 ± 1.07	3.47	0.12	1.64 ± 0.15	18.85 ± 0.12	2.68 ± 0.29
G0.50+0.19	5.06 ± 1.97	–6.00 ± 0.47	6.06 ± 1.34	1.46 ± 0.61	4.06	1.69	1.98 ± 0.21	–6.14 ± 0.22	4.27 ± 0.56
G0.55–0.85	77.38 ± 0.51	16.96 ± 0.02	5.51 ± 0.03	67.09 ± 3.57	5.34	0.28	7.74 ± 0.23	17.52 ± 0.05	3.55 ± 0.13
G0.84+0.18	1.50 ± 0.15	6.98 ± 0.09	1.86 ± 0.22	1.90 ± 1.01	3.39	1.80	0.49 ± 0.06	5.91 ± 0.17	2.74 ± 0.41
G1.15–0.12	10.51 ± 2.44	–18.70 ± 0.10	4.50 ± 0.48	4.43 ± 1.08	5.30	1.29	1.11 ± 0.14	–17.23 ± 0.26	4.11 ± 0.61
G2.54+0.20	12.42 ± 0.77	9.58 ± 0.05	2.97 ± 0.14	1.99 ± 0.49	1.13	0.28	3.26 ± 0.49	10.10 ± 0.17	2.82 ± 0.22
G5.89–0.39	82.33 ± 0.54	9.31 ± 0.00	4.94 ± 0.04	43.75 ± 1.52	3.19	0.11	7.31 ± 0.16	9.31 ± 0.04	4.08 ± 0.10
G5.90–0.43	32.27 ± 0.43	6.44 ± 0.03	3.88 ± 0.06	32.00 ± 2.35	4.14	0.30	4.09 ± 0.15	6.97 ± 0.06	3.41 ± 0.15
G5.90–0.44	14.70 ± 0.17	9.40 ± 0.00	6.30 ± 0.09	10.06 ± 0.63	4.79	0.30	1.65 ± 0.08	9.46 ± 0.05	2.04 ± 0.11
G6.54–0.11	1.68 ± 0.10	13.60 ± 0.14	4.74 ± 0.32	1.64 ± 0.53	4.45	1.43	–	–	–
G6.61–0.08	0.37 ± 0.12	6.92 ± 0.12	0.73 ± 0.26	0.22 ± 0.80	0.77	2.78	0.58 ± 0.12	7.72 ± 0.23	2.24 ± 0.45
G8.14+0.23	19.53 ± 0.69	19.77 ± 0.07	5.00 ± 0.09	13.88 ± 1.08	4.26	0.33	1.53 ± 0.17	19.18 ± 0.20	3.60 ± 0.44
G8.67–0.36	36.95 ± 0.42	34.80 ± 0.00	5.31 ± 0.08	10.76 ± 0.92	2.75	0.23	5.86 ± 0.15	34.80 ± 0.05	4.11 ± 0.13
G8.68–0.37	51.08 ± 1.76	37.25 ± 0.05	7.33 ± 0.14	25.66 ± 1.06	7.57	0.31	5.58 ± 0.18	37.22 ± 0.07	5.35 ± 0.22
G9.62+0.19	32.98 ± 1.05	3.46 ± 0.09	5.93 ± 0.22	10.99 ± 1.11	3.24	0.33	3.60 ± 0.10	4.45 ± 0.06	4.53 ± 0.15
G9.99–0.03	11.48 ± 0.23	48.97 ± 0.05	4.88 ± 0.11	11.75 ± 1.28	5.26	0.57	0.80 ± 0.08	48.90 ± 0.11	2.29 ± 0.26
G10.29–0.13	13.66 ± 0.57	12.04 ± 0.06	4.53 ± 0.25	12.64 ± 1.39	5.16	0.57	2.40 ± 0.34	13.70 ± 0.23	3.60 ± 0.27
G10.30–0.15	57.13 ± 0.69	12.47 ± 0.03	6.79 ± 0.11	16.98 ± 2.03	4.26	0.51	5.33 ± 0.18	12.99 ± 0.07	4.38 ± 0.18
G10.32–0.16	25.81 ± 0.54	11.77 ± 0.04	4.18 ± 0.06	7.17 ± 0.96	1.94	0.26	1.89 ± 0.12	12.15 ± 0.09	2.63 ± 0.20
G10.34–0.14	26.98 ± 0.42	12.30 ± 0.03	4.02 ± 0.05	15.73 ± 1.11	3.02	0.21	2.30 ± 0.16	12.22 ± 0.10	2.98 ± 0.25
G10.44–0.02	14.79 ± 1.25	75.26 ± 0.12	5.59 ± 0.24	8.20 ± 1.14	5.45	0.76	1.66 ± 0.09	75.41 ± 0.12	4.58 ± 0.30
G10.47+0.03	82.39 ± 1.56	67.13 ± 0.03	8.19 ± 0.12	66.60 ± 2.53	10.14	0.39	4.93 ± 0.17	67.05 ± 0.11	6.82 ± 0.28
G10.48+0.03	42.33 ± 0.44	65.90 ± 0.03	8.04 ± 0.10	24.62 ± 1.02	8.36	0.35	3.40 ± 0.22	66.15 ± 0.17	6.26 ± 0.50
G10.63–0.33	13.79 ± 0.22	–3.63 ± 0.04	4.55 ± 0.09	13.80 ± 1.21	4.78	0.42	2.17 ± 0.19	–4.14 ± 0.13	2.85 ± 0.18
G10.63–0.38	98.30 ± 0.41	–3.74 ± 0.01	7.59 ± 0.04	95.57 ± 1.65	7.86	0.14	11.06 ± 0.26	–3.14 ± 0.05	6.04 ± 0.22
G11.50–1.49	23.72 ± 1.56	10.07 ± 0.12	4.55 ± 0.14	9.26 ± 1.72	2.70	0.50	1.16 ± 0.08	10.26 ± 0.07	2.03 ± 0.16
G11.94–0.15	12.02 ± 0.27	41.90 ± 0.05	4.58 ± 0.13	12.18 ± 1.40	4.73	0.54	1.53 ± 0.20	42.60 ± 0.29	4.46 ± 0.67
G11.94–0.62	35.97 ± 0.94	38.54 ± 0.04	4.49 ± 0.06	15.97 ± 1.26	3.14	0.25	3.57 ± 0.24	37.89 ± 0.09	4.00 ± 0.28
G11.99–0.27	4.15 ± 0.26	58.62 ± 0.12	4.62 ± 0.38	2.41 ± 1.02	4.48	1.89	0.66 ± 0.09	59.66 ± 0.26	4.47 ± 0.94
G12.03–0.03	4.14 ± 0.26	111.04 ± 0.11	3.48 ± 0.25	4.49 ± 1.55	4.38	1.51	0.69 ± 0.09	110.47 ± 0.20	3.57 ± 0.55
G12.18–0.12	10.42 ± 0.21	25.91 ± 0.04	5.13 ± 0.13	11.26 ± 0.75	5.92	0.39	1.25 ± 0.19	26.51 ± 0.67	9.12 ± 1.73
G12.21–0.09	16.76 ± 4.94	24.24 ± 0.06	3.49 ± 0.38	7.26 ± 1.31	5.31	0.96	1.02 ± 0.13	23.82 ± 0.20	3.10 ± 0.50
G12.68–0.18	6.55 ± 0.43	58.40 ± 0.10	3.46 ± 0.29	6.97 ± 1.14	3.93	0.64	1.15 ± 0.09	56.46 ± 0.10	2.70 ± 0.26
G12.72–0.22	13.39 ± 0.51	34.87 ± 0.06	4.85 ± 0.14	10.31 ± 0.72	5.87	0.41	2.62 ± 0.36	34.19 ± 0.05	2.63 ± 0.21
G12.89+0.49	23.06 ± 2.21	33.63 ± 0.10	3.83 ± 0.13	9.80 ± 1.25	3.26	0.42	2.23 ± 0.10	33.34 ± 0.07	3.09 ± 0.16
G12.91–0.26	43.31 ± 1.43	38.88 ± 0.11	11.35 ± 0.39	12.79 ± 4.43	5.30	1.84	4.81 ± 0.14	36.95 ± 0.05	3.55 ± 0.12
G14.60+0.02	12.32 ± 4.70	25.64 ± 0.30	7.23 ± 1.41	4.93 ± 0.99	9.59	1.93	3.14 ± 0.67	24.74 ± 0.41	6.27 ± 0.74
G14.99–0.70	47.84 ± 0.81	18.75 ± 0.04	6.35 ± 0.07	40.16 ± 1.20	6.74	0.20	2.19 ± 0.15	18.70 ± 0.16	4.75 ± 0.38
G15.03–0.68	73.99 ± 0.70	19.68 ± 0.02	4.14 ± 0.03	64.16 ± 1.52	4.08	0.10	5.29 ± 0.13	19.50 ± 0.03	2.89 ± 0.09
G15.03–0.71	14.81 ± 0.26	20.98 ± 0.03	4.49 ± 0.11	10.71 ± 0.80	5.23	0.39	0.63 ± 0.10	20.97 ± 0.45	5.44 ± 0.99

Table 6 – continued

Source	HCO ⁺ Gaussian Fits ^α			HCO ⁺ Integrated Lines ^β			H ¹³ CO ⁺ Gaussian Fits		
	T _{MB} dv (K km s ⁻¹)	V _{LSR} (km s ⁻¹)	δV (km s ⁻¹)	T _{MB} dv (K km s ⁻¹)	Equivalent Width (km s ⁻¹)	Peak T _{MB} (K)	T _{MB} dv (K km s ⁻¹)	V _{LSR} (km s ⁻¹)	δV (km s ⁻¹)
G16.59–0.05	29.29 ± 0.57	59.34 ± 0.03	3.56 ± 0.05	21.53 ± 1.17	3.35	0.18	2.26 ± 0.17	59.86 ± 0.12	3.28 ± 0.30
G16.86–2.16	43.08 ± 0.47	17.89 ± 0.02	4.78 ± 0.04	18.48 ± 1.03	3.42	0.19	5.48 ± 0.39	17.77 ± 0.12	3.54 ± 0.20
G19.36–0.03	10.22 ± 0.93	27.85 ± 0.12	5.19 ± 0.43	5.76 ± 1.18	4.67	0.96	1.56 ± 0.09	26.73 ± 0.08	2.89 ± 0.19
G19.47+0.17	24.36 ± 1.02	18.91 ± 0.09	7.56 ± 0.24	15.90 ± 1.63	7.25	0.74	3.96 ± 0.75	19.71 ± 0.13	4.49 ± 0.50
G19.49+0.15	6.19 ± 0.23	22.70 ± 0.07	4.06 ± 0.20	6.07 ± 1.01	4.29	0.72	0.74 ± 0.07	23.03 ± 0.13	3.12 ± 0.37
G19.61–0.13	9.32 ± 0.22	57.14 ± 0.06	4.75 ± 0.13	9.41 ± 1.10	5.30	0.62	0.42 ± 0.09	56.94 ± 0.45	3.77 ± 0.74
G19.70–0.27	1.30 ± 0.21	44.28 ± 0.21	2.54 ± 0.49	1.56 ± 1.14	4.87	3.56	0.90 ± 0.15	42.99 ± 0.00	2.58 ± 0.52
G21.88+0.01	7.22 ± 1.24	22.88 ± 0.09	4.96 ± 0.49	3.96 ± 0.97	6.70	1.64	0.87 ± 0.12	23.34 ± 0.27	4.16 ± 0.73
G22.36+0.07	9.79 ± 0.23	84.39 ± 0.05	4.12 ± 0.12	10.54 ± 1.13	4.87	0.52	0.81 ± 0.08	84.07 ± 0.13	2.55 ± 0.28
G23.26–0.24	8.90 ± 0.59	61.67 ± 0.19	5.89 ± 0.31	7.53 ± 1.13	5.11	0.77	1.02 ± 0.06	61.50 ± 0.08	2.81 ± 0.21
G23.44–0.18	62.71 ± 1.99	100.62 ± 0.14	10.50 ± 0.16	37.47 ± 1.91	8.11	0.41	3.51 ± 0.17	101.59 ± 0.10	4.25 ± 0.24
G23.71–0.20	5.33 ± 0.27	68.36 ± 0.11	4.89 ± 0.47	5.67 ± 1.15	6.44	1.31	0.95 ± 0.07	68.96 ± 0.13	3.86 ± 0.30
G24.79+0.08	30.46 ± 0.67	111.06 ± 0.05	6.14 ± 0.10	14.46 ± 1.12	4.40	0.34	4.43 ± 0.16	110.51 ± 0.07	4.24 ± 0.18
G24.85+0.09	5.60 ± 0.14	109.00 ± 0.04	3.32 ± 0.10	3.95 ± 0.72	3.48	0.63	0.43 ± 0.06	108.88 ± 0.22	3.01 ± 0.50
G25.65+1.05	28.07 ± 0.39	42.30 ± 0.04	5.20 ± 0.09	14.29 ± 1.43	3.68	0.37	4.04 ± 0.15	42.43 ± 0.06	3.63 ± 0.16
G25.71+0.04	10.12 ± 0.33	98.97 ± 0.07	4.28 ± 0.16	10.17 ± 1.64	4.64	0.75	1.08 ± 0.07	98.73 ± 0.10	3.19 ± 0.22
G25.83–0.18	31.55 ± 1.03	94.04 ± 0.04	4.67 ± 0.09	11.94 ± 1.32	3.42	0.38	1.89 ± 0.06	93.39 ± 0.06	3.32 ± 0.13
G28.15+0.00	6.18 ± 1.20	98.70 ± 0.32	6.56 ± 0.61	3.47 ± 0.85	6.92	1.69	1.11 ± 0.07	98.59 ± 0.08	2.45 ± 0.18
G28.20–0.05	35.26 ± 0.56	96.37 ± 0.07	11.59 ± 0.26	30.18 ± 1.41	11.21	0.53	2.71 ± 0.13	95.58 ± 0.09	3.93 ± 0.24
G28.28–0.36	8.31 ± 0.22	48.73 ± 0.06	5.68 ± 0.23	7.53 ± 0.82	6.93	0.76	0.89 ± 0.07	48.87 ± 0.10	2.88 ± 0.26
G28.31–0.39	2.49 ± 0.07	85.52 ± 0.03	2.17 ± 0.07	2.55 ± 0.29	2.42	0.28	1.50 ± 0.19	86.18 ± 0.23	3.92 ± 0.62
G28.83–0.25	20.19 ± 0.60	87.06 ± 0.05	5.71 ± 0.19	6.10 ± 0.98	3.74	0.60	2.15 ± 0.14	87.06 ± 0.11	3.36 ± 0.23
G29.87–0.04	22.83 ± 0.24	100.90 ± 0.02	4.38 ± 0.06	15.45 ± 1.18	4.20	0.32	1.47 ± 0.10	100.91 ± 0.10	3.20 ± 0.23
G29.96–0.02	25.51 ± 1.43	96.86 ± 0.11	4.72 ± 0.15	14.50 ± 1.75	4.04	0.49	2.88 ± 0.14	97.63 ± 0.07	2.83 ± 0.17
G29.98–0.04	–	–	–	20.68 ± 1.55	10.55	0.79	1.80 ± 0.07	101.57 ± 0.05	2.63 ± 0.12
G30.59–0.04	6.52 ± 0.30	42.21 ± 0.11	5.36 ± 0.33	6.99 ± 1.69	5.51	1.33	1.73 ± 0.13	41.81 ± 0.14	3.88 ± 0.34
G30.71–0.06	9.85 ± 1.15	88.19 ± 0.22	5.27 ± 0.46	5.87 ± 1.51	4.68	1.20	6.40 ± 1.28	92.85 ± 0.34	5.53 ± 0.52
G30.76–0.05	8.53 ± 0.36	89.25 ± 0.12	5.72 ± 0.29	8.46 ± 2.08	6.55	1.61	2.92 ± 0.33	93.00 ± 0.00	5.38 ± 0.73
G30.78+0.23	4.22 ± 0.18	41.99 ± 0.07	3.29 ± 0.17	4.37 ± 1.00	3.82	0.88	0.90 ± 1.25	41.80 ± 0.00	1.55 ± 1.03
G30.79+0.20	5.40 ± 0.44	81.25 ± 0.20	6.98 ± 0.93	3.94 ± 1.11	5.53	1.56	1.10 ± 0.07	81.59 ± 0.09	3.17 ± 0.23
G30.82–0.05	29.34 ± 2.36	96.57 ± 0.23	6.58 ± 0.33	22.29 ± 1.50	6.56	0.44	4.09 ± 0.28	96.61 ± 0.12	4.08 ± 0.37
G30.82+0.28	5.33 ± 0.18	97.28 ± 0.05	3.16 ± 0.14	5.75 ± 1.16	3.73	0.76	0.42 ± 0.05	97.77 ± 0.12	1.98 ± 0.26
G30.90+0.16	14.43 ± 0.33	105.53 ± 0.06	5.07 ± 0.13	14.02 ± 1.85	5.56	0.73	1.46 ± 0.21	106.17 ± 0.20	3.19 ± 0.61
G31.28+0.06	23.88 ± 4.52	109.33 ± 0.06	4.38 ± 0.27	6.81 ± 0.90	4.38	0.58	3.23 ± 0.13	109.40 ± 0.08	4.18 ± 0.18
G31.41+0.31	34.55 ± 4.10	97.50 ± 0.00	6.41 ± 0.37	10.04 ± 2.13	5.27	1.12	1.46 ± 0.20	96.66 ± 0.25	3.49 ± 0.53
G316.81–0.06	42.43 ± 0.94	–38.16 ± 0.05	5.27 ± 0.06	29.12 ± 1.43	4.56	0.22	2.72 ± 0.24	–38.68 ± 0.20	4.21 ± 0.44
G318.95–0.20	25.29 ± 0.39	–34.28 ± 0.02	3.49 ± 0.06	18.94 ± 1.14	3.72	0.22	3.57 ± 0.13	–34.53 ± 0.05	2.72 ± 0.10
G323.74–0.26	30.18 ± 1.21	–49.50 ± 0.05	4.27 ± 0.11	14.16 ± 1.26	3.71	0.33	2.56 ± 0.11	–49.65 ± 0.05	2.61 ± 0.13
G331.28–0.19	18.06 ± 1.12	–89.64 ± 0.08	5.78 ± 0.61	6.38 ± 1.30	3.84	0.78	2.39 ± 0.10	–88.11 ± 0.08	4.02 ± 0.20
G332.73–0.62	12.48 ± 0.20	–50.22 ± 0.03	3.52 ± 0.07	13.29 ± 1.30	4.01	0.39	0.72 ± 0.09	–50.20 ± 0.09	1.46 ± 0.20

^α Gaussian fits to HCO⁺ lines constrained by the sides of the line only. Any absorption dips were masked from the fitting routine.^β Integrated area under the line measured by summing the channels between suitable velocity limits.

Table 7. Gaussian fits to HCO^+ line wings and blended lines.

Source ^α	$T_{MB} dv$ (K km s ⁻¹)	V_{LSR} (km s ⁻¹)	δV (km s ⁻¹)	Code ^β
G0.32–0.20	9.31 ± 0.61	18.48 ± 0.24	11.88 ± 0.93	w
G0.50+0.19	16.77 ± 2.11	26.02 ± 2.57	43.07 ± 6.50	b
G0.55–0.85	9.84 ± 0.54	22.23 ± 0.09	4.77 ± 0.31	b
G2.54+0.20	7.76 ± 1.04	9.76 ± 0.14	5.57 ± 0.53	w
G5.89–0.39	47.45 ± 3.11	10.91 ± 0.49	26.75 ± 1.21	w
G6.61–0.08	31.45 ± 0.74	–1.75 ± 0.27	23.98 ± 0.66	b
G8.67–0.36	14.61 ± 1.71	35.23 ± 0.25	13.20 ± 0.91	w
G9.62+0.19	18.37 ± 0.96	4.29 ± 0.14	11.47 ± 0.46	w
G10.30–0.15	35.38 ± 0.95	11.11 ± 0.10	11.90 ± 0.24	w
G10.32–0.16	13.88 ± 0.76	12.23 ± 0.10	7.48 ± 0.36	w
G10.34–0.14	9.74 ± 0.65	11.50 ± 0.22	9.95 ± 0.57	w
G10.44–0.02	3.17 ± 0.23	65.92 ± 0.16	4.87 ± 0.46	b
G10.48+0.03	15.60 ± 1.62	66.12 ± 0.21	13.80 ± 0.96	w
G10.63–0.38	11.26 ± 1.07	3.10 ± 0.23	6.40 ± 0.42	b
G11.50–1.49	10.89 ± 0.74	13.64 ± 0.68	20.46 ± 1.35	w
G11.94–0.15	1.38 ± 0.27	47.20 ± 0.21	2.66 ± 0.64	b
G11.99–0.27	4.76 ± 0.45	59.83 ± 0.72	17.40 ± 2.38	w
G12.91–0.26	23.45 ± 1.28	42.54 ± 0.67	27.54 ± 1.72	w
G14.60+0.02	2.04 ± 0.13	37.93 ± 0.14	4.05 ± 0.32	b
G15.03–0.71	3.13 ± 0.98	18.50 ± 1.09	8.96 ± 1.03	wb
G16.86–2.16	16.41 ± 0.95	18.44 ± 0.25	17.59 ± 0.83	w
G19.47+0.17	2.64 ± 0.41	27.23 ± 0.24	4.07 ± 0.87	b
G19.49+0.15	1.22 ± 0.26	17.71 ± 0.38	3.35 ± 0.83	b
G19.70–0.27	1.05 ± 0.26	38.51 ± 0.37	3.32 ± 1.08	b
G24.79+0.08	13.17 ± 0.98	111.37 ± 0.21	17.71 ± 1.39	w
G24.79+0.08	0.43 ± 0.17	102.30 ± 0.00	1.35 ± 0.62	b
G24.85+0.09	3.54 ± 0.34	106.81 ± 0.55	12.36 ± 1.32	w
G25.65+1.05	26.85 ± 0.72	41.34 ± 0.23	21.83 ± 0.65	w
G25.83–0.18	10.03 ± 0.60	95.08 ± 0.63	21.70 ± 2.14	w
G28.83–0.25	11.14 ± 0.62	89.25 ± 0.31	13.98 ± 0.77	w
G29.87–0.04	12.86 ± 1.06	99.72 ± 0.26	11.71 ± 0.76	w
G29.96–0.02	6.74 ± 2.49	95.76 ± 1.91	12.24 ± 2.88	w
G29.96–0.02	1.86 ± 1.27	103.48 ± 0.44	3.59 ± 1.37	b
G29.98–0.04	12.09 ± 4.09	101.74 ± 1.65	17.45 ± 2.12	w
G29.98–0.04	14.02 ± 2.71	95.81 ± 0.15	6.72 ± 0.60	b
G30.71–0.06	7.74 ± 1.51	99.09 ± 2.40	27.20 ± 3.69	w
G30.79+0.20	3.87 ± 0.34	93.62 ± 0.33	8.34 ± 0.91	b
G30.82–0.05	8.22 ± 1.35	104.12 ± 0.00	5.01 ± 0.71	b
G318.95–0.20	6.26 ± 1.00	–31.33 ± 0.53	6.73 ± 0.68	w
G323.74–0.26	7.64 ± 0.69	–48.52 ± 0.46	15.47 ± 1.97	w
G332.73–0.62	4.14 ± 0.33	–56.21 ± 0.20	5.56 ± 0.54	b
G331.28–0.19	11.29 ± 0.72	–89.34 ± 0.42	18.51 ± 1.26	w

^α The fits quoted here were *subtracted* from the HCO^+ spectra before analysing the line profile. We assume that these blended lines and line wings do not come from the same region as the $H^{13}CO^+$ emission.

^β ‘w’ denotes a Gaussian fit to a HCO^+ (1–0) line wing, ‘b’ denotes a Gaussian fit to a blended HCO^+ (1–0) line.

Table 8. Parameters Derived from CH₃CN.

Source	T _{rot} ^α (K)	Column Density ^β (×10 ¹³ m ⁻²)	Notes ^γ	Source	T _{rot} ^α (K)	Column Density ^β (×10 ¹³ m ⁻²)	Notes ^γ
G0.55−0.85	60 ± 3	7.2 ± 2.2	5 M R	G12.91−0.26	68 ± 16	2.0 ± 0.6	b M −
	63 ± 8	3.2 ± 1.0	6	G14.60+0.02	63 ± 12	0.8 ± 0.2	5 M R
	60 ± 6	6.2 ± 1.9	b	G15.03−0.68	78 ± 16	1.2 ± 0.4	6 M −
G5.89−0.39	56 ± 4	3.5 ± 1.1	5 − R	G16.86−2.16	36 ± 16	1.1 ± 0.3	5 M −
G5.90−0.43	46 ± 8	3.3 ± 1.0	5 M −		43 ± 9	1.1 ± 0.3	6
	45 ± 6	2.1 ± 0.6	6		41 ± 13	1.1 ± 0.3	b
	45 ± 7	2.5 ± 0.8	b	G19.47+0.17	55 ± 13	2.5 ± 0.8	5 M −
G5.90−0.44	32 ± 5	0.6 ± 0.2	5 − −	G23.44−0.18	47 ± 7	2.2 ± 0.7	5 M −
G8.14+0.23	42 ± 10	0.7 ± 0.2	5 M R		47 ± 6	2.0 ± 0.6	6
G8.67−0.36	43 ± 3	2.6 ± 0.8	5 M R		47 ± 7	2.1 ± 0.6	b
G8.68−0.37	44 ± 3	2.2 ± 0.7	5 M −	G24.79+0.08	74 ± 9	6.7 ± 2.0	5 M −
G9.62+0.19	60 ± 9	4.1 ± 1.2	5 M R		81 ± 9	6.3 ± 1.9	6
G9.99−0.03	38 ± 29	0.3 ± 0.1	5 M −		77 ± 9	6.5 ± 1.9	b
G10.29−0.13	30 ± 8	1.2 ± 0.4	5 M −	G25.83−0.18	53 ± 8	2.5 ± 0.8	5 M −
G10.30−0.15	32 ± 8	1.8 ± 0.5	5 M R		55 ± 19	2.0 ± 0.6	6
G10.32−0.16	56 ± 19	1.6 ± 0.5	5 M −		53 ± 15	2.3 ± 0.7	b
	53 ± 24	0.5 ± 0.1	6	G28.20−0.05	74 ± 26	2.6 ± 0.8	5 M R
	55 ± 22	0.6 ± 0.2	b	G29.96−0.02	75 ± 23	3.5 ± 1.1	5 M R
G10.34−0.14	30 ± 12	0.7 ± 0.2	5 M −		116 ± 39	4.8 ± 1.4	6
	28 ± 7	0.8 ± 0.2	6		86 ± 32	3.9 ± 1.2	b
	28 ± 10	0.8 ± 0.2	b	G30.71−0.06	51 ± 9	3.7 ± 1.1	5 M R
G10.48+0.03	64 ± 13	3.3 ± 1.0	5 M −		75 ± 16	3.3 ± 1.0	6
G10.63−0.38	52 ± 5	4.8 ± 1.4	5 M R		57 ± 13	3.5 ± 1.1	b
	55 ± 7	3.1 ± 0.9	6	G30.76−0.05	29 ± 14	0.4 ± 0.1	5 M −
	53 ± 6	3.9 ± 1.2	b	G30.82−0.05	52 ± 6	6.6 ± 2.0	5 M −
G11.94−0.62	32 ± 9	1.1 ± 0.3	5 M R		78 ± 9	7.7 ± 2.3	6
G12.68−0.18	44 ± 18	0.8 ± 0.2	5 M −		61 ± 8	7.1 ± 2.1	b
	84 ± 35	1.6 ± 0.5	6	G31.41+0.31	98 ± 13	8.3 ± 2.5	6 M R
	52 ± 28	0.9 ± 0.3	b	G316.81−0.06	73 ± 24	1.7 ± 0.5	5 M −
G12.72−0.22	28 ± 17	0.4 ± 0.1	5 − −	G318.95−0.20	55 ± 9	1.8 ± 0.5	5 M −
G12.89+0.49	131 ± 53	5.2 ± 1.6	5 M −	G323.74−0.26	67 ± 12	2.3 ± 0.7	5 M −
G12.91−0.26	28 ± 18	0.6 ± 0.2	5 M −	G331.28−0.19	74 ± 16	2.7 ± 0.8	5 M −
	94 ± 15	5.0 ± 1.5	6				

^α Quoted errors in T_{rot} are the 1σ uncertainties arising from the least-squares straight line fit to the rotational diagram.

^β Quoted errors in N are ~30%, arising from the relative calibration error between observations.

^γ Results marked with a ‘6’ or a ‘5’ were derived from individual J=(6−5) or J=(5−4) rotational ladders respectively. Where we could derive T_{rot} and N from both J-transitions we calculated the weighted average, marked with a ‘b’ in the notes column. ‘R’ denotes associated 8.6 GHz radio emission and ‘M’ marks a methanol maser site.

Table 9. Comparison of CH_3CN Parameters to Previous Surveys

	This Paper	Pankonin et al. (2001)	Hatchell et al. (1998)	Olmi et al. (1993)	Churchwell et al. (1992)
Antenna Diameter:	22-m	10-m	15-m	30-m	30-m
Beam Size:	35''	35''	21'', 14''	21'', 17'', 12''	25'', 11''
(Assumed) source size:	35''	35''	< 1.5''	5''	10''

Transitions Used:	Rotational Temperature, T_{rot} (K)				
	(5–4), (6–5)	(12–11)	(13–12) and (19–18)	(6–5), (8–7), (12–11)	(6–5), (12–11)
G5.89-0.39	56	75	d	–	84
G9.62+0.19	60	135	119 and 65	123	–
G10.30-0.15	32	n	n	34	–
G10.47+0.03	d	196	87 and 134	d	–
G10.63-0.38	53	103	–	–	102
G11.94-0.62	32	n	–	–	d
G12.21-0.09	n	d	d	72	–
G15.03-0.68	78	n	–	52	–
G25.65+1.05	166	197	–	–	–
G29.96-0.02	86	150	114 and 141	–	144
G31.41+0.31	98	292	149 and 142	–	372

Transitions Used:	Column Density, $N_{\text{col}} (\times 10^{13} \text{ cm}^{-2})$				
	(5–4), (6–5)	(12–11)	(13–12)	(6–5), (8–7), (12–11)	(6–5), (12–11)
G5.89-0.39	3.5	2.3	d	–	13
G9.62+0.19	4.1	1.8	2	10.6	–
G10.30-0.15	1.8	n	n	11.9	–
G10.47+0.03	d	8	13	d	–
G10.63-0.38	3.9	2.2	–	–	11
G11.94-0.62	1.2	n	–	–	d
G12.21-0.09	n	d	d	7.1	–
G15.03-0.68	0.8	n	–	2.6	–
G25.65+1.05	d	0.74	–	–	–
G29.96-0.02	3.9	1.8	3	–	6
G31.41+0.31	8.3	8	5	–	17

d = CH_3CN detected but no meaningful rotational temperature or column-density could be derived.

n = CH_3CN was not detected.

– = Source not observed.

Table 10. Parameters derived from analysis of the HCO⁺ and H¹³CO⁺ lines.

Source	$\tau(\text{H}^{13}\text{CO}^+)^{\alpha}$	$N(\text{H}^{13}\text{CO}^+)$ ($\times 10^{13} \text{ cm}^{-2}$)	$N(\text{HCO}^+)^{\beta}$ ($\times 10^{14} \text{ cm}^{-2}$)	Source	$\tau(\text{H}^{13}\text{CO}^+)^{\alpha}$	$N(\text{H}^{13}\text{CO}^+)$ ($\times 10^{13} \text{ cm}^{-2}$)	$N(\text{HCO}^+)^{\beta}$ ($\times 10^{14} \text{ cm}^{-2}$)
G0.32-0.20	0.050	2.0	10.1	G16.86-2.16	0.130	7.0	34.9
G0.50+0.19	0.040	2.4	12.1	G19.36-0.03	0.040	1.9	9.6
G0.55-0.85	0.190	10.2	50.8	G19.47+0.17	0.070	4.9	24.5
G0.84+0.18	0.010	0.6	3.0	G19.49+0.15	0.020	0.9	4.5
G1.15-0.12	0.020	1.3	6.7	G19.61-0.13	0.010	0.5	2.5
G2.54+0.20	0.100	4.1	20.4	G19.70-0.27	0.030	1.1	5.4
G5.89-0.39	0.150	9.4	47.1	G21.88+0.01	0.020	1.1	5.3
G5.90-0.43	0.100	5.1	25.7	G22.36+0.07	0.030	1.0	4.9
G5.90-0.44	0.070	2.0	10.2	G23.26-0.24	0.030	1.2	6.2
G6.61-0.08	0.020	0.7	3.5	G23.44-0.18	0.070	4.3	21.7
G8.14+0.23	0.030	1.9	9.3	G23.71-0.20	0.020	1.1	5.7
G8.67-0.36	0.120	7.4	37.2	G24.79+0.08	0.090	5.5	27.6
G8.68-0.37	0.090	7.0	34.8	G24.85+0.09	0.010	0.5	2.6
G9.62+0.19	0.060	4.5	22.3	G25.65+1.05	0.090	5.1	25.3
G9.99-0.03	0.030	1.0	4.8	G25.71+0.04	0.030	1.3	6.5
G10.29-0.13	0.050	3.0	14.7	G25.83-0.18	0.050	2.3	11.6
G10.30-0.15	0.100	6.7	33.5	G28.15+0.00	0.040	1.4	6.8
G10.32-0.16	0.060	2.3	11.7	G28.20-0.05	0.060	3.3	16.6
G10.34-0.14	0.060	2.8	14.2	G28.28-0.36	0.020	1.1	5.4
G10.44-0.02	0.030	2.0	10.0	G28.31-0.39	0.030	1.8	9.1
G10.47+0.03	0.060	6.1	30.4	G28.83-0.25	0.050	2.6	13.2
G10.48+0.03	0.040	4.2	20.8	G29.87-0.04	0.040	1.8	9.0
G10.63-0.33	0.060	2.7	13.4	G29.96-0.02	0.080	3.6	17.9
G10.63-0.38	0.160	14.3	71.4	G29.98-0.04	0.060	2.2	11.1
G11.50-1.49	0.050	1.4	7.1	G30.59-0.04	0.040	2.1	10.6
G11.94-0.15	0.030	1.9	9.3	G30.71-0.06	0.100	8.0	40.1
G11.94-0.62	0.070	4.4	22.2	G30.76-0.05	0.040	3.6	17.8
G11.99-0.27	0.010	0.8	3.9	G30.78+0.23	0.050	1.1	5.5
G12.03-0.03	0.020	0.8	4.2	G30.79+0.20	0.030	1.3	6.7
G12.18-0.12	0.010	1.5	7.5	G30.82-0.05	0.080	5.1	25.5
G12.21-0.09	0.030	1.2	6.2	G30.82+0.28	0.020	0.5	2.6
G12.68-0.18	0.030	1.4	7.0	G30.90+0.16	0.040	1.8	8.9
G12.72-0.22	0.080	3.3	16.3	G31.28+0.06	0.060	4.0	19.9
G12.89+0.49	0.060	2.8	13.7	G31.41+0.31	0.030	1.8	8.9
G12.91-0.26	0.110	6.1	30.4	G316.81-0.06	0.050	3.3	16.7
G14.60+0.02	0.040	3.8	19.2	G318.95-0.20	0.110	4.5	22.5
G14.99-0.70	0.040	2.7	13.3	G323.74-0.26	0.080	3.2	15.9
G15.03-0.68	0.160	6.8	34.1	G331.28-0.19	0.050	2.9	14.7
G15.03-0.71	0.010	0.8	3.8	G332.73-0.62	0.040	0.9	4.4
G16.59-0.05	0.060	2.8	13.9				

^α We assumed an excitation temperature of 15 K when calculating the optical depth of the H¹³CO⁺ (1-0) line. Excitation temperatures derived from the HCO⁺ (1-0) line were anomalously low, most likely as a result of beam dilution.

^β A Galactic gradient in the ¹²C/¹³C isotope ratio has been observed, ranging from 20 to 70, however, there is considerable uncertainty in these results. The [HCO⁺]/[H¹³CO⁺] ratio may also be affected by chemistry. We prefer to use an average value of 50 when calculating the column density of HCO⁺.

Table 11. Parameters of the MSX red and MSX dark sources.

Source	CH ₃ CN	HCO ⁺	H ¹³ CO ⁺	21 μm	8 μm	Maser	Radio	Profile	Wings	T _{rot}
MSX-red										
G12.18-0.12	n	y	y	y	n	y	n	–	–	–
G12.21-0.09	n	y	y	y	n	y	n	blue	–	–
G14.60+0.02	y	y	y	y	n	y	n	–	–	63
G24.79+0.08	y	y	y	y	n	y	n	red	y	77
G25.71+0.04	y	y	y	y	n	y	n	–	–	–
G28.83-0.25	y	y	y	y	n	y	n	red	y	–
G30.79+0.20	y	y	y	y	d	y	n	–	–	–
G323.74-0.26	y	y	y	y	n	y	n	red	y	67
MSX-dark										
G0.26+0.01	y	y	y	d	d	n	n	–	–	–
G2.54+0.20	n	y	y	n	d	y	n	blue	y	–
G8.68-0.37	y	y	y	n	d	y	n	blue	–	43
G10.44-0.02	y	y	y	n	d	y	n	blue	–	–
G10.48+0.03	y	y	y	n	d	y	n	–	y	64
G14.99-0.70	y	y	y	n	d	n	n	–	–	–
G23.44-0.18	y	y	y	n	d	y	n	red	–	47
G25.83-0.18	y	y	y	n	d	y	n	blue	y	53
G29.98-0.04	y	y	y	n	d	y	n	–	y	–
G30.71-0.06	y	y	y	d	d	y	b	blue	y	57
G30.82-0.05	y	y	y	n	d	y	n	blue	–	61
G332.73-0.62	y	y	y	d	d	y	n	–	–	–